Stony Brook University

New designs and characterization techniques for thin-film solar cells

A Dissertation presented

by

Yutong Pang

to

The Graduate School

in Partial Fulfillment of the

Requirements

for the Degree of

Doctor of Philosophy

in

Physics

Stony Brook University

August 2016

Stony Brook University

The Graduate School

Yutong Pang

We, the dissertation committe for the above candidate for the

Doctor of Philosophy degree, hereby recommend

acceptance of this dissertation

Matthew Eisaman - Dissertation Advisor
Assistant Professor, Department of Electrical & Computer Engineering

Xu Du - Chairperson of Defense
Associate Professor, Department of Physics and Astronomy

Thomas Allison
Assistant Professor, Department of Physics and Astronomy

Matthew Reuter
Assistant Professor, Department of Applied Mathematics & Statistics

This dissertation is accepted by the Graduate School

Nancy Goroff
Interim Dean of the Graduate Schooll

Abstract of the Dissertation

New designs and characterization techniques for thin-film solar cells

by

Yutong Pang

Doctor of Philosophy

in

Physics

Stony Brook University

2016

This thesis presents a fundamentally new thin-film photovoltaic design and develops several novel characterization techniques that improve the accuracy of thin-film solar cell computational models by improving the accuracy of the input data.

We first demonstrate a novel organic photovoltaic (OPV) design, termed a "Slot OPV", in which the active layer is less than 50 nm; We apply the principles of slot waveguides to confine light within the active layer. According to our calculation, the guided-mode absorption for a 10nm thick active layer equal to the absorption of normal incidence on an OPV with a 100nm thick active layer. These results, together with the expected

improvement in charge extraction for ultrathin layers, suggest that slot OPVs can be designed with greater power conversion efficiency than today's state-of-art OPV architectures if practical challenges, such as the efficient coupling of light into these modes, can be overcome.

The charge collection probability, i.e. the probability that charges generated by absorption of a photon are successfully collected as current, is a critical feature for all kinds of solar cells [13, 28, 35]. While the electron-beam-induced current (EBIC) method has been used in the past to successfully reconstruct the charge collection probability [17, 37, 43, 61], this approach is destructive and requires time-consuming sample preparation. We demonstrate a new nondestructive optoelectronic method to reconstruct the charge collection probability by analyzing the internal quantum efficiency (IQE) data that are measured on copper indium gallium diselenide (CIGS) thin-film solar cells. We further improve the method with a parameter-independent regularization approach. Then we introduce the Self-Constrained Ill-Posed Inverse Problem (SCIIP) method, which improves the signal-to-noise of the solution by using the regularization method with system constraints and optimization via an evolutionary algorithm.

For a thin-film solar cell optical model to be an accurate representation of reality, the measured refractive index profile of the solar cell used as input

to the model must also be accurate. We describe a new method for reconstructing the depth-dependent refractive-index profile with high spatial resolution in thin photoactive layers. This novel technique applies to any thin film, including the photoactive layers of a broad range of thin-film photovoltaics.

Together, these methods help us improve the measurement accuracy of the depth profile within thin-film photovoltaics for optical and electronic properties such as refractive index and charge collection probability, which is critical to the understanding, modeling, and optimization of these devices.

TABLE OF CONTENTS

II   New Reconstruction Techniques for improved model accuracy

49

LISTING OF FIGURES

ACKNOWLEDGMENTS

Firstly, I would like to express my sincere gratitude to my advisor Matthew Eisaman for his mentorship and support of my Ph.D. study, for his patience, immense knowledge, and kindness. It was an honor working with him, and I will never forget these days.

I would also like to thank the other members of my thesis and oral exam committee: Prof. Xu Du, Prof. Philip Allen, Prof. Thomas Allison and Prof. Matthew Reuter. Their insight feedback and comment on my annual oral exam guided this work in the right direction.

Also, I would like to thank my fellow labmates: Dr. Ahsan Ashraf, Dr. Nanditha Dissanayake, Matthew Bossart and Jan Folkson, for the stimulating discussions and all the fun we have had in the last four years.

Throughout this entire time, I benefitted greatly from close interaction with the staff members from BNL|Center for Functional Nanomaterials, most notably Dr. Charles Black, Dr. Fernando Camino, Dr. Lihua Zhang, Dr. Mingzhao Liu and Dr. Chang-Yong Nam.

Last but not the least, I would like to thank my parents and grandparents who taught me the value of hard work and to be an independent thinker, for their love and encouragement. This thesis is dedicated to you.

Citations to Previously Published Work

Parts of Chapter 2 have been published as

- Pang, Yutong, Nanditha Dissanayake, and Matthew D. Eisaman."Guided-mode absorption in ultrathin organic photovoltaics." Photovoltaic Specialists Conference (PVSC), 2012 38th IEEE. IEEE, 2012.

- Camino, Fernando E., et al. "Characterization of plasmonic hole arrays as transparent electrical contacts for organic photovoltaics using high-brightness Fourier transform methods." Journal of modern optics 61.21 (2014): 1735-1742.

- Eisaman, Matthew, Yutong Pang, and Nanditha Dissanayake."Thin-film photovoltaic device with optical field confinement and method for making same." U.S. Patent Application No. 14/399,800.

- Pang, Yutong, M. Bossart, and M. D. Eisaman. "Index-matched IWKB

method for the measurement of spatially varying refractive index profiles within thin-film photovoltaics." Optics express 22.101 (2014): A188-A197.

Parts of Chapter 3 have been published as

- Dissanayake, D. M., et al. "Mapping spatially resolved charge collection probability within P3HT: PCBM bulk heterojunction photovoltaics." Advanced Energy Materials 4.2 (2014)

Parts of Chapter 4 have been published as

- Pang, Y. T., et al. "Reconstruction of the charge collection probability in a CIGS solar cell by the regularization method." Photovoltaic Specialist Conference (PVSC), 2015 IEEE 42nd. IEEE, 2015.

- Dissanayake, D. M. N. M., et al. "Guided-mode quantum efficiency: A novel optoelectronic characterization technique." Review of Scientific Instruments 83.11 (2012): 114704.

- Dissanayake, Nanditha, et al. "Hyperspectral guided-mode quantum efficiency: A novel characterization technique for thin-film photovoltaics." 2013 IEEE 39th Photovoltaic Specialists Conference (PVSC). IEEE, 2013.

Parts of Chapter 6 have been published as

- Pang, Yutong, M. Bossart, and M. D. Eisaman. "Index-matched IWKB method for the measurement of spatially varying refractive index profiles within thin-film photovoltaics." Optics express 22.101 (2014): A188-A197.

Parts of Chapter 7 have been published as

- Pang, Yutong, and Matthew D. Eisaman. "Measuring refractive index profiles within thin-film photovoltaics with high spatial resolution using the modified IM-IWKB method." 2014 IEEE 40th Photovoltaic Specialist Conference (PVSC). IEEE, 2014.

CHAPTER 1

INTRODUCTION

Transferring energy directly from the sunlight into electricity using photovoltaic (PV) technology is being widely recognized as a critical component of future global energy production [5]. Since the first inorganic crystalline silicon solar cell which had an efficiency about 6% , was developed at Bell Laboratories[10], there have been substantial improvements in silicon cell performance, culminating in the 25% value [23], which is already close to the theoretical predicted upper limit of 30% [22, 65]. For all conventional inorganic solar cell, there is a p-n junction. The p side is doped with a material (typically boron) that accepts electrons from the silicon, while the n side is doped with a material (typically phosphorous) that donates electrons to the silicon. Upon connecting the p and n-type materials, electrons flow from the n-type to p-type region (and holes from the p to n type region), leaving behind positively charged ions on the n-side near the junction and negatively charged ions on the p-side. This depletion of charges from the junction continues until the diffusion of charges due to their concentration

1

gradient is balanced by the electric field established in the so-called depletion region. Every carrier formed within the depletion region or that diffuses to the depletion region will be directed by the electric field to the proper electrode.

In addition to inorganic solar cells whose operation we have described above, so-called organic solar cells that employ organic semiconductors as the absorbing layer have the potential to be a less expensive alternative. Although organic-based photovoltaics hold promise as a low-cost, highly scalable and flexible technology, the conversion efficiency of the organic polymer and small molecule based photovoltaics (OPVs) has been limited due to the combined challenges of extremely short ($\sim$10 nm) exciton diffusion length, bimolecular recombination, and low free-carrier mobility [36]; Significant increases at least 1.5 times in device performance are needed for economic viability [45, 49]. While an ultrathin ($<$ 50 nm) active layer (the layer in which absorption of photons leads to photogenerated charge carriers that are extracted from the photovoltaic (PV) cell for power generation) is desirable to overcome the above challenges, the optical absorption decreases significantly for active layer thicknesses on the order of the exciton diffusion length ($\sim$10nm)[84]. Complete light absorption in OPV cells typically requires active layer thicknesses of at least 150 nm, a length scale one order of magnitude larger than the exciton diffusion length. To solve this problem, we introduced the ultrathin slot organic photovoltaics structure.

1.1 ULTRATHIN SLOT ORGANIC PHOTOVOLTAICS DESIGN

Research over the past ten years has shown the potential for metallic nanostructures to improve light absorption and thereby the efficiency of thin film photovoltaics by using the plasmon resonance of the nanostructure to effectively trap incoming light within the active layer of the cell [4, 9, 20]. These approaches typically have nanostructures somewhere throughout the cell to efficiently couple incident sunlight into these guided modes. A typical OPV architecture for this case is shown in Fig. 1.1.1 (a).These approaches do not allow sufficiently light confinement of the electromagnetic field in ultrathin active layers, which themselves are necessary to gain increased IQE. In other words, as the active layer thickness is decreased to improve the IQE, the absorption of guided modes becomes poor (no better than absorption of normal incidence light for similarly thin active layers). Therefore with such an approach, it is not possible to improve the overall cell performance by decreasing the active layer thickness to improve IQE, while keeping absorption as strong as for a thick active layer by scattering incident light into tightly confined waveguide modes of the active layer. Further to this fundamental drawback, work done on field enhancement using metal nanoparticles within the active layer[38, 50], has other significant challenges such as charge trapping, shunting, and increase in the overall cost.

In Chapter 1, we demonstrate a novel organic photovoltaic (OPV) design, termed a "slot OPV", that applies the principles of slot waveguides to confine light within the ultrathin (< 50nm) active layer of an OPV. We have
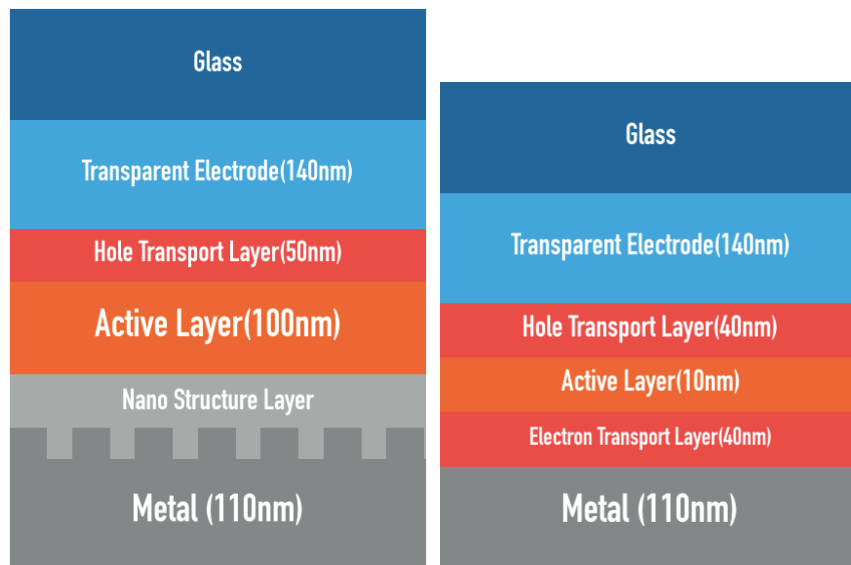
(a) Typical OPV architecture **(b)** Ultrathin Slot OPV design

Figure 1.1.1: (a). Typical OPV architecture for the prior art: Glass / Transparent Electrode(140nm) / Hole Transport Layer (50nm) with refractive index n = 1.8 / Active Layer(100nm) / Nanostructured Layer / Metal electrode (110nm) (b). Ultrathin Slot OPV design: Glass / Transparent Electrode(140nm) / Hole Transport Layer (40nm) with high refractive index n = 3.5 / Active Layer(100nm) / Electron Transport Layer (40nm) with high refractive index n = 3.5 / Metal electrode (110nm)

used the Transfer Matrix Method (TMM) [12, 80] to solve for the guided modes and calculate the electromagnetic field (E-field) distribution of these modes in various OPV waveguide structures, including archetype OPV structures (glass/ITO/PEDOT: PSS/P3HT: PCBM/Al), and novel structures whose layers have unique combinations of optical and electrical properties. Our calculations demonstrate that a slot OPV can be designed with guided-mode absorption for a 10nm thick active layer equal to the absorption of normal incidence on an OPV with a 100nm thick active layer. These results, together with the expected improvement in charge extraction for ultrathin layers, suggest that slot OPVs can be designed with greater power conversion efficiency than today's state-of-art OPV architectures if practical challenges, such as the efficient coupling of light into these modes, can be overcome. For instance, the absorption fraction for TE_0 guided mode within a 10nm active layer is around four times better in our slot OPV design than the typical OPV architecture.

1.2   Charge Collection Probability Reconstruction

In the previous section, we already discussed that a ultrathin active layer could improve the charge collection probability. The charge collection probability $\phi(z)$ which defined as the probability that a carrier generated by light absorption at position z of the device will be collected and therefore contribute to the light-generated current is a critical feature for all kinds of solar cells. It mainly depends on the distance that a light-generated carrier
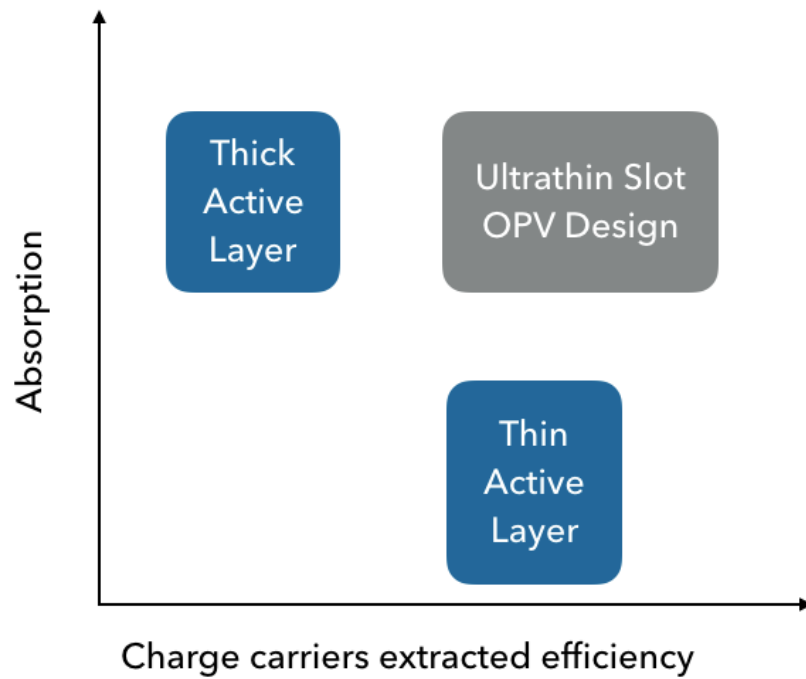
Figure 1.1.2: Comparison of absorption and charge collection for the typical OPV architecture (blue) and the ultrathin slot OPV design (gray). For typical OPV architecture, the thick active layer can achieve high absorption, but low charge extraction efficiency. On the other hand, the thin active layer can achieve high charge extraction efficiency, but low absorption. For ultrathin slot OPV design, we can achieve both high absorption and high charge extraction efficiency if we can solve practical challenges such as efficiently coupling light into these modes.

must travel compared to the diffusion length, but also dependent on the surface properties of the devices [28]. Knowing the charge collection probability will also give us some information about the surface and junction properties of the device and show us how to optimize the device. In this section, we will discuss how to measure the charge collection probability using a non-destructive optoelectronic method.

While the electron-beam-induced current (EBIC) method has been used in the past to successfully reconstruct the charge collection probability [17, 37, 43, 61], this approach is destructive and requires time-consuming sample preparation, it also changes the charges state of defects within CIGS absorber layer, resulting in a change of $\phi(z)$ with electron energy [37], in violation of the assumption of the $\phi(z)$ is the same for all measurements.

In Chapter 3, we described a novel optical and non-destructive method for the direct reconstruction of the charge collection probability $\phi(z)$ from the measurement of internal quantum efficiency (IQE) as a function of wavelength $(\eta(\lambda))$.We also used this method to reconstruct the charge collection probability for a standard CIGS solar cell as shown in Fig. 3.2.1. Letting $G(z, \lambda)$ be the normalized probability distribution per unit length of creating an electron-hole pair at depth z within the active layer for the laser wavelength λ, the basic relation between the depth-dependent charge-collection probability $\phi(z)$ within the device and the externally

7

measured IQE ($\eta(\lambda)$) is

$$\eta(\lambda) = \int\limits_{0}^{t_{CIGS}} G(z,\lambda)\phi(z)dz \qquad (1.1)$$

Where t_{CIGS} is the thickness of CIGS active layer.

After, we measured $\eta(\lambda)$ for different wavelengths, $\phi(z)$ is obtained by using Eq.1.1 above to find the best fit in the following parametrized functional forms [37] using least-squares fit with gradient decent:

when $0 \leq z < z_{SCR}$

$$\varphi(z) = 1 \qquad (1.2)$$

when $z_{SCR} \leq z \leq z_{Mo}$

$$\varphi(z) = \frac{\left(\frac{1}{L_{eff}}\cosh[\frac{z-z_{Mo}}{L_{eff}}] - \frac{S_{Mo}}{D}\sinh[\frac{z-z_{Mo}}{L_{eff}}]\right)}{\frac{1}{L_{eff}}\cosh[\frac{z_{Mo}-z_{SCR}}{L_{eff}}] + \frac{S_{Mo}}{D}\sinh[\frac{z_{Mo}-z_{SCR}}{L_{eff}}]} \qquad (1.3)$$

Where z_{Mo} represents the Position of CIGS/Mo interface, z_{SCR} represents the depth of space-charge region, L_{eff} represents minority carrier diffusion length, S_{Mo} represents the recombination velocity at CIGS/Mo and D represents diffusion constant.

Our nondestructive optoelectronic method avoids the drawbacks from EBIC method, allows the bias voltage, bias light, and temperature to be easily varied, and also allows $\phi(z)$ to be reconstructed for a wider range of material, including those which would be damaged by EBIC. However, this method is a model and parameter dependent method, which means we need to know the true form of the charge collection probability model beforehand.

Any deviation from the model will lead to error in the reconstruction.

In Chapter 4, we further improve the method with a parameter-independent approach for the direct reconstruction of the charge collection probability $\phi(z)$ from the measurement of IQE as a function of wavelength ($\eta(\lambda)$). This inversion process is an ill-posed problem, but a stable solution can be found by applying the regularization method.

The linear problem is well-posed if it satisfies the following three requirements [27]:

- The problem must have a solution.

- There must be only one solution to the problem.

- The solution must depend continuously on the data.

If the inverse problem violates one or more of these requirements, it is said to be ill-posed or ill-conditioned [51].

Application of the regularization technique to an ill-posed inverse problem is only possible if the data noise is within a specified range; the noise can both come from measurement and model. To solve an ill-posed inverse problem to which regularization cannot be applied due to noise, in Chapter 5 we introduce the Self-Constrained Ill-Posed Inverse Problem (SCIIP) method, which improves the signal-to-noise of the solution by using the regularization method with system constraints and optimization via an evolutionary algorithm. The source code for the SCIIP method can be found on Github: https://github.com/wstcpyt/InverseProblemPackage [53]. Imagine that we have performed measurements, the results of which are

9

denoted b, but we know that these measurements are composed of the actual quantity of interest plus noise. Our method relies on the fact that the actual quantity of interest without noise (denoted $b_{noiseless}$) must exist in the parameter space neighborhood of the measured result b_{meas}, and that $b_{noiseless}$ will give a better reconstruction (the smaller residual, the better) than b_{meas}. Our method searches the space $b \pm \eta$ (where η defines the search space, and should be on the order of the standard deviation of the noise to successfully find $b_{noiseless}$) using a Cellular Evolutionary Algorithm (CEA) to find the b that minimizes the residual. We then feed this new b into the regularization process, which yields a result x that is closer to the true x than would be obtained by just feeding b_{meas} directly into the regularization method. This work has the potential to improve the accuracy of inverse problem reconstruction solutions in a wide range of fields.

The self-constrained ill-posed inverse problem (SCIIP) method has the potential to improve the accuracy of inverse problem reconstruction solution in a wide range of fields, including subsurface mapping in geology [69], image reconstruction in astronomy or medicine [2, 14], and depth profiling of solar cells and other thin-film stacks [15, 55, 75]. In future work, a more efficient optimization method other than Cellular Evolutionary Algorithm should also be developed to apply this work to 2D case.

1.3 High resolution depth-dependent refractive index profile reconstruction

For a thin-film solar cell optical model to be an accurate representation of reality, the measured refractive index profile of the solar cell used as input to the model must also be accurate. For the optical modeling in previous sections, we are assuming that the refractive index are constant values within the active layer. However, in real practice, the refractive index usually depends on the depth of the active layer.

In Chapters 6 and 7 we describe a new method for reconstructing the depth-dependent refractive-index profile with high spatial resolution in thin photoactive layers which we refer to as index-matched IWKB (IM-IWKB), While the Inverse Wentzel-Kramers-Brillouin (IWKB) method has been used in the past to successfully reconstruct RIPs of various films [8, 11, 64, 85], this approach is only valid for relatively thick (larger than 2 μm) films for visible wavelengths, since the number of points in the reconstructed RIP is equal to the number of modes supported by the film at that wavelength. For the ultra-thin layers relevant to many thin-film photovoltaics (typically 100 nm – 200 nm for OPVs, for example), it is either impossible to reconstruct the profile at all, or the result of the reconstruction has poor spatial resolution due to the low number of guided modes. In contrast, my new IM-IWKB technique applies to any thin film, including the photoactive layers of a broad range of thin-film photovoltaics.

The IM-IWKB method described in this thesis deposits a relatively

thick (1-10 μm) index-matched, non-absorbing layer below the thin photoactive layer of interest, and then applies the IWKB method to this system, resulting in a spatial resolution for the reconstruction of the RIP that is improved by more than a factor of ten compared to the traditional IWKB without the use of an index-matched layer. While RIPs for such thin layers can be obtained using spectroscopic ellipsometry with multiple-layer models [3, 21], our approach requires no free parameters, which is a significant advantage compared to the parameterized, model-based technique used in ellipsometry. This allows much higher spatial resolution using our approach compared to ellipsometry, where the number of free parameters necessarily increases with the desired spatial resolution.

Part I

Optical Modeling of Photovoltaics for improved solar cell devices

Chapter 2

Guided Mode Absorption in Ultrathin Organic Photovoltaics

2.1 Introduction

In this chapter, we describe a novel organic photovoltaic (OPV) design, termed a "slot OPV", that applies the principles of slot waveguides to confine light within the ultrathin (<50nm) active layer of an OPV. Our calculations demonstrate that a "slot OPV" can be designed with guided-mode absorption for a 10 nm thick active layer equal to the absorption of normal incidence on an OPV with a 100nm thick active layer. These results, together with the expected improvement in charge extraction for ultrathin layers, suggest that slot OPVs can be designed with greater power conversion efficiency than today's state-of-art OPV architectures if practical challenges, such as the efficient coupling of light into these modes, can be overcome.

2.2 ULTRATHIN ORGANIC PHOTOVOLTAICS

Organic Photovoltaics (OPVs) hold promise as a low cost, highly scalable and sustainable photovoltaic technology, but significant increases in device performance are needed for economic viability [45, 49]. The conversion efficiency of OPVs has been limited due to the combined charge-extraction challenges of short exciton diffusion length (10nm in organic polymers), bimolecular recombination and disorder-induced low free carrier mobility[30, 36, 41, 44, 45].

While an ultrathin (< 50 nm) active layer is desirable to overcome the above challenges, the optical absorption for normal incidence decreases significantly for active layer thicknesses on the order of the exciton diffusion length [84]. For a traditional OPVs design, complete light absorption typically requires active layer thickness of at least 150nm, a length scale one order of magnitude larger than the exciton diffusion length. Research over the past ten years has shown the potential for metallic nanostructures to improve light absorption and thereby the efficiency of thin film photovoltaics by using the plasmon resonance of the nanostructure to effectively trap incoming light within the active layer of the cell [4, 9, 20]. These approaches typically have nanostructures somewhere throughout the cell to efficiently couple incident sunlight into these guided modes. A typical OPV architecture for this case is shown in Fig. 1.1.1. These approaches do not provide sufficient light confinement of the electromagnetic field in ultrathin active layers, which themselves are necessary to gain increased IQE. In other

words, as the active layer thickness is decreased to improve the IQE, the absorption of guided modes becomes poor (no better than absorption of normal incidence light for similarly thin active layers). Therefore with such an approach, it is not possible to improve the overall cell performance by decreasing the active layer thickness to improve IQE, while keeping absorption as strong as for a thick active layer by scattering incident light into tightly confined waveguide modes of the active layer. Further to this fundamental drawback, work done on field enhancement using metal nanoparticles within the active layer[38, 50], has other significant challenges such as charge trapping, shunting, and increase in the overall cost.

Recent work suggests the possibility of achieving strong absorption in ultrathin active layers by efficiently scattering the incident light into guided optical modes [7, 20, 24, 59, 82]. In this chapter, we will apply this concept to develop a novel organic photovoltaic design.

2.3   Guided Modes in Ultrathin Organic Photovoltaics

An important question to ask is whether light trapping in guided modes can enable significant optical absorption for ultrathin OPVs. Guided mode are defined such that their electromagnetic fields in the top layer (cover) and the bottom layer (substrate) of the waveguide decay exponentially with distance, thereby confining the energy in the waveguide structure [12, 78]. To this end, in this chapter, we calculate the fraction of the incident power that can be absorbed by the active layer for each guided mode and normally incident light in several OPV architectures. The primary purpose of this

analysis is to determine the maximum possible absorption for each guided mode, and thereby determine whether light trapping via guided modes is a potentially promising approach for enabling ultrathin active-layer OPVs.

2.4 Transfer Matrix Method

To compare guided-mode and normal-incidence absorption for various OPV structures, we need to calculate the electromagnetic field propagation within a multilayer structure like that shown in Fig. 2.4.1, both for the case of normally-incident light and for the case of guided modes.

We use the Transfer Matrix Method (TMM) [12, 78] to calculate the electromagnetic field distribution within the OPV structure for a given field incident upon the cell.

TMM is a very useful method for determining the steady-state solution to Maxwell's equations in the thin film multilayer structure, and it is addressed extensively in the literature[6, 12, 31, 32, 70].

Here we consider the stack of J films illustrated in Fig. 2.4.2. The interface of the films is labeled from 1 to $J - 1$, the cover and substrate interface is labeled as c and s. There is material variation in only x direction; we only need to solve the Maxwell's equations for transverse-electric (TE) and transverse-magnetic (TM) polarization.

The Transfer Matrix relates the field amplitudes U_j and V_j at x_j to the
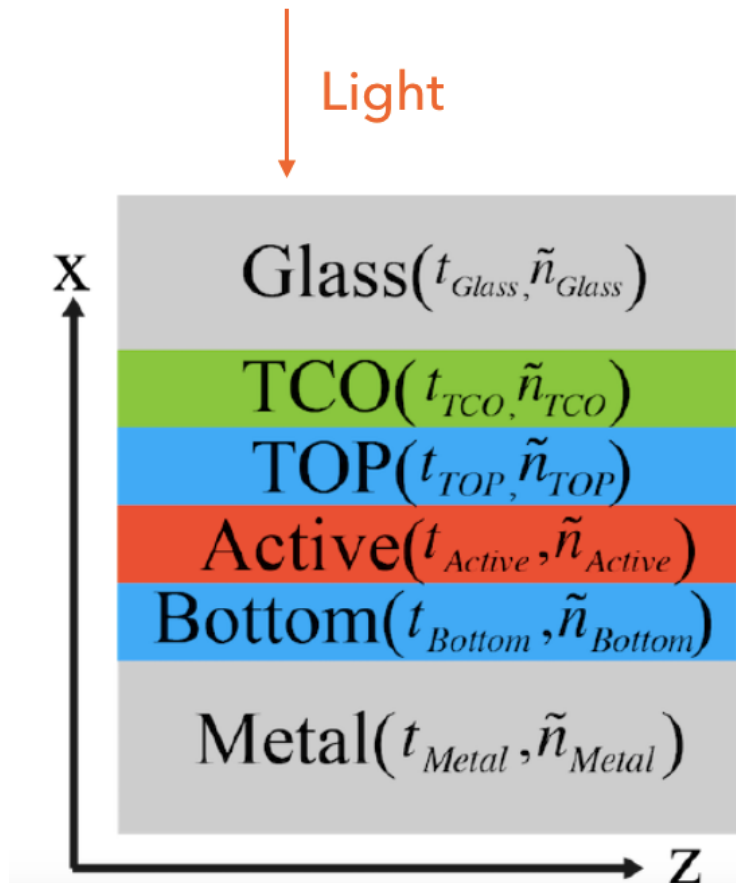
Figure 2.4.1: Generic Schematic of an OPV. Each layer has a thickness t, and a complex refractive index $\tilde{n} = n + ik$. TCO=Transparent Conductive Oxide and "Active" denotes the active layer intended for photon absorption. Top layer is the hole transport layer and bottom layer is electron transport layer.
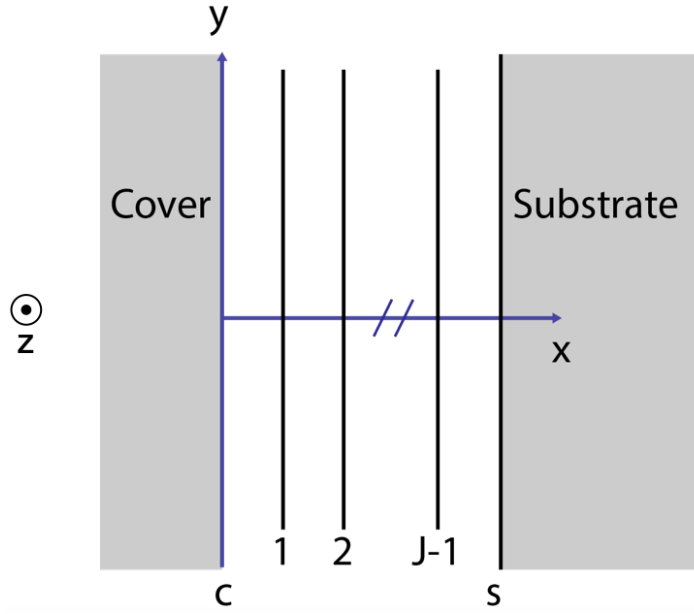
Figure 2.4.2: Generic Schematic of the multilayer film structure; it consists of J layers of films lying between the semi-infinite cover and substrate media.

corresponding amplitudes at a a second point x_{j-1} can be expressed as[12]:

$$
\begin{pmatrix} U_{j-1} \\ V_{j-1} \end{pmatrix} = M_j \begin{pmatrix} U_j \\ V_j \end{pmatrix}
\tag{2.1}
$$

Transfer matrix M_j takes the form:

$$
M_j = \begin{pmatrix} \cos \Phi_j & \frac{-i}{\gamma_j} \sin \Phi_j \\ -i\gamma_j \sin \Phi_j & \cos \Phi_j \end{pmatrix}
\tag{2.2}
$$

where

$$
\begin{aligned}
\Phi_j &= k\alpha_j(x_j - x_{j-1}) \\
\alpha &= n\cos\theta = (n^2 - \beta^2)^{1/2} \\
\beta &= n\sin\theta.
\end{aligned}
\tag{2.3}
$$

19

Polarization	γ	U	V	W	Other Field Components
TE	α/z_0	E_z	$-H_y$	H_x	$H_z = E_y = E_x = 0$
TM	$\alpha z_0/n^2$	H_z	E_y	$-E_x$	$E_z = H_y = H_x = 0$

Table 2.4.1: Polarization parameters for TE and TM mode

γ, U, V, W have different meanings for the two polarizations - the details are shown in the table. 2.4.1. For the TE polarization, there is no electric field in the direction of propagation. For the TM polarization, there is no magnetic field in the direction of propagation The transfer matrix for a stack consisting of J films is given by the product of the respective transfer matrices for each individual layers:

$$M = \prod_{j=1}^{J} M_j = \begin{pmatrix} m_{11} & m_{12} \\ m_{21} & m_{22} \end{pmatrix} \tag{2.4}$$

2.4.1 Guided Mode

Guided modes occur when the fields in the cover and substrate decay exponentially. We use TMM to solve for the guided modes of the OPV structure by obtaining the transfer equations, and solving these transfer equations to obtain the model dispersion function:

$$\chi_M(\beta) = \gamma_c m_{11} + \gamma_c \gamma_s m_{12} + m_{21} + \gamma_s m_{22} = 0 \tag{2.5}$$

where β is the effective index of refraction, with zeros of this equation corresponding to guided modes[12]. We can solve this equation using Newton's method [42]. Once the effective index is known, this can be substituted back into our expression for the electric field using TMM to calculate the electric field at any point in the structure for a given guided mode [57]. Once the electric field of each guided mode is known, we calculate the relative energy absorbed by each layer in the OPV structure. This allows us to calculate the fraction of light in a given guided mode that is absorbed by the active layer.

2.5 Results and Discussion

2.5.1 Standard OPV Structure

First, we determine the baseline optical absorption by calculating the absorption fraction for guided modes and normally incident light in the OPV structure shown in Fig. 2.4.1 with materials and thicknesses given by: glass/TCO (140 nm) / Top (40 nm) / Active (5 - 150 nm) / Metal (200 nm), where the TCO is indium tin oxide (ITO), the "Top" layer is poly(3 ,4-ethylenedioxythiophene):poly(styrenesulfonate) (PEDOT:PSS), the "Active" layer is poly(3- hexylthiophene):[6,6]-phenyl Cwbutyric acid methyl ester ($P3HT : PCBM$), the "Bottom" layer is absent, and the "Metal" layer is Al. The glass cover is treated as semi-infinite in our calculations. We shall refer to this structure as a "standard OPV" throughout this section.

Fig. 2.5.2 (a)-(c) show the fraction of light absorbed (at wavelengths

21

λ=400 nm, 600 nm, and 800 nm, respectively) in the active layer of this standard OPV architecture for $P3HT : PCBM$ active-layer thicknesses ranging from 5 nm - 150 nm. This calculation is performed for all guided modes that exist at a given thickness/wavelength combination, and also for normally incident light. At each active-layer thickness, the results shown in Fig. 2.5.2(a)-(c) are discretely integrated, from 300 nm to 800 nm with 50 nm wide bins, over the AM1.5G [52] solar spectrum to obtain the total absorption for each mode at a given active-layer thickness - this result is shown in Fig. 2.5.2(d). The solar spectrum depends on the day and the location, AM1.5 solar spectrum are introduced to allow the performance comparison of photovoltaic devices from different manufacturers and research laboratories. The standard solar spectral is shown in Fig. 2.5.1 [18]. We limit the upper wavelength of the integration to 800 nm because the absorption strength of $P3HT : PCBM$ drops steeply at 650 nm, and is very small for wavelengths larger than about 650 nm. The TM2 mode shown in Fig. 2.5.2(d) but not seen in Fig. 2.5.2(a)-(c) comes from the wavelength range 300 nm - 400nm. To obtain the plot shown in 2.5.2(d), for a given active layer thickness, modes that exist over only part of the integration range of 300 nm - 800 nm are simply integrated over the part of the spectrum where they do exist.

From Fig. 2.5.2, we see that TM modes have a consistently larger absorption fraction than normal incidence, with the relative difference increasing greatly as the active layer thickness decreases. Fig. 2.5.2(d) shows

22
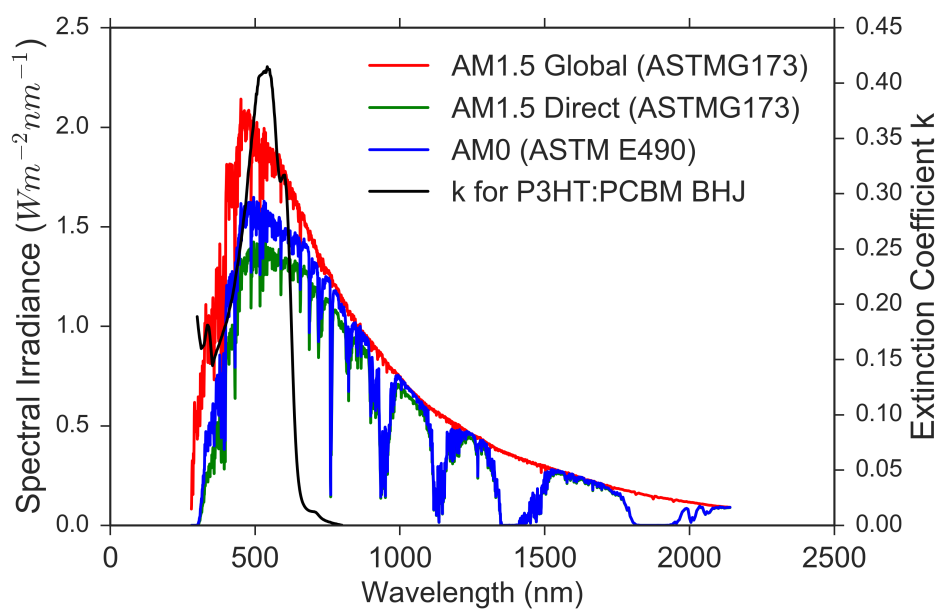
Figure 2.5.1: Standard Solar spectrum for space and terrestrial use with extinction coefficient k for P3HT:PCBM bulk heterojunction. The left-y axis shows the spectral irradiance for red, green and blue lines. The right-y axis shows the extinction coefficient k for black line.
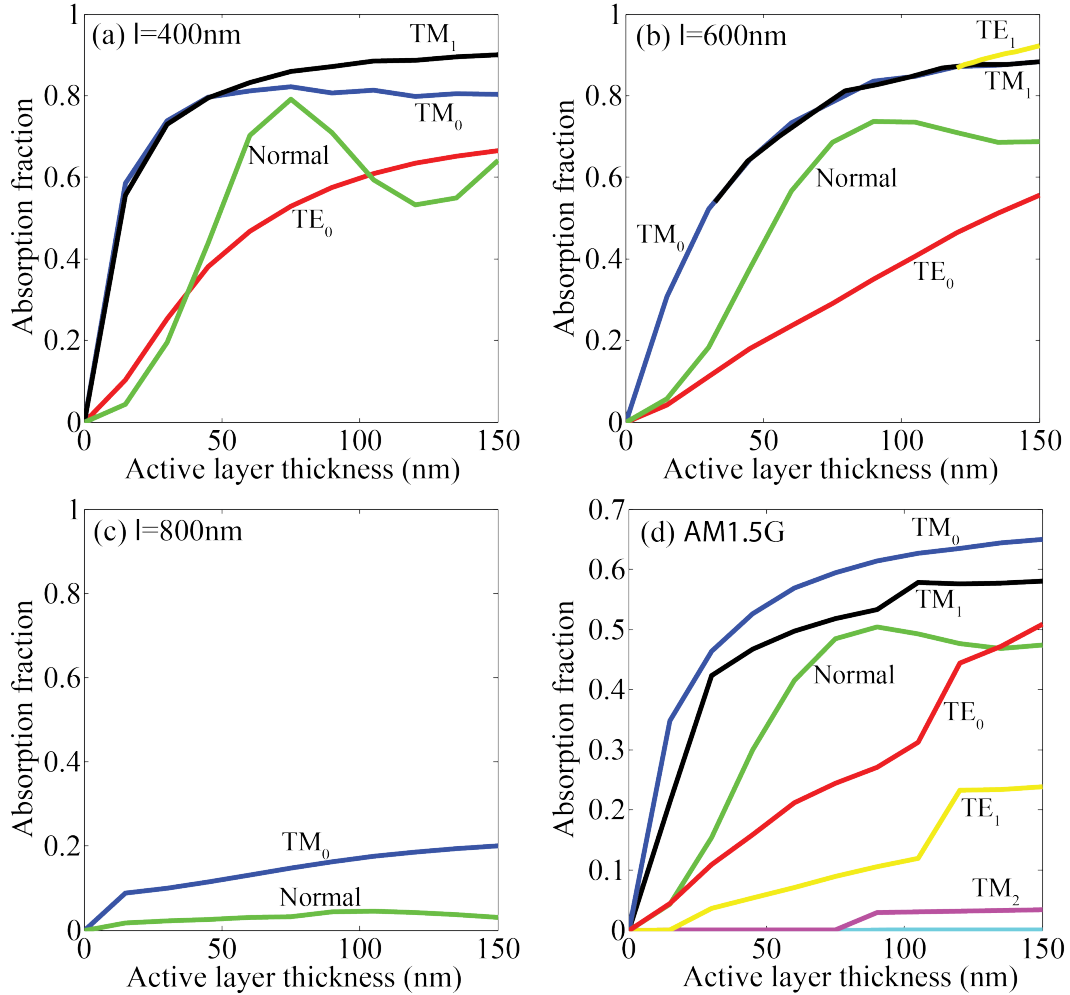
Figure 2.5.2: Absorption fraction (power absorbed in active layer/incident power) vs. thickness of the active layer ($P3HT : PCBM$) for the "standard OPV" architecture (see text), for wavelength: (a) 400 nm, (b) 600 nm, (c) 800 nm, and (d) Average over AM1. 5G solar spectrum[52]. The calculation performed using Lumerical FDTD for the 2D case with perfect matched layer (PML) boundaries absorb electromagnetic waves incident upon them [67]. I also used C++ to develop my own version of FDTD simulation package [66]. The refractive index for all materials are also obtained from the Lumerical database. For each guided mode, all the incident energy is assumed to be perfectly coupled into the mode of interest. For normal incidence, the incident energy is the energy incident on the glass/ITO interface.

that while the TM_0 absorption fraction asymptotically approaches 0.65 at an active layer thickness of 150 nm (a value approximately 1.4 times larger than that for normal incidence), at an active layer thickness of 10 nm, the TM_0 absorption fraction is approximately eight times larger than that of normal incidence. This behavior makes physical sense, since for active layers thicker than about 100 nm, most of the normally incident light is absorbed and so less room for improvement exists by guiding modes in the active layer. For ultrathin active layers on the order of 10 nm thick, however, very little light is absorbed for normal incidence, meaning that any mode that is tightly confined to the active layer (such as TM_0 in this case) will have greatly enhanced absorption relative to the normal incidence case. From Fig. 2.5.2(d), we see that a TM_0 guided mode in a standard OPV cell with a 40 nm-thick active layer will have the same absorption fraction as normal incidence on a standard cell with a 100 nm-thick active layer. An equivalent absorption fraction in a thinner active layer has the potential to result in an OPV with improved overall power conversion efficiency due to the improved charge extraction properties of the thinner active layers. As we shall see in the next section, the thickness of the active layer can be reduced even further with the optimization of the optical properties of the Top and Bottom hole- and electron-transport layers (see Fig. 2.4.1).

From Fig. 2.5.2 we also see that in contrast to the behavior of TM modes, the TE modes have absorption fractions that are less than or equal to the normal incidence case. The strong absorption of TM modes relative to TE modes is due to the stronger confinement of TM modes in the active

layer of the cell for the standard OPV architecture [40, 60]. As we shall discuss in the next section, by carefully choosing the optical properties and thicknesses of the Top and Bottom hole- and electron transport layers (see Fig. 2.4.1), the absorption fraction of both TM and TE modes can be increased by enabling tighter confinement of the guided mode in the active layer of the cell.

2.5.2 Ultrathin OPV with Embedded High-Index Layers

Recent investigations of so-called "slot waveguides" have demonstrated the strong confinement of light in layers on the order of 10 nm $-$ 50 nm thick by sandwiching a thin relatively low-index layer between two layers of higher index [1]. We introduce a novel OPV design that applies the principles of slot waveguides to tightly confine light within the active layer of an ultrathin OPV structure. Regarding the generic schematic shown in Fig. 2.4.1, both the Top and Bottom hole- and electron-transport layers of such a structure have large values of refractive index relative to the active-layer index. We shall refer to this structure as a "slot OPV" throughout the paper.

We first turn our attention to Fig. 2.5.3(a), which considers the case of Top and Bottom layers with n_{Top}=n_{Bot}=3.5, and $k_{Top} = k_{Bot} = 0$. We see that the absorption fractions of the guided modes in a slot OPV are equal to the $t_{active} = 100$ nm absorption fraction of about 0.5 for the "Normal (standard)" case for a slot OPV active-layer thickness of (20 nm, 40 nm) for the (TM_0, TE_0) modes, respectively. This is a very important result, as it suggests that strong guided-mode absorption is possible for ultrathin active

26
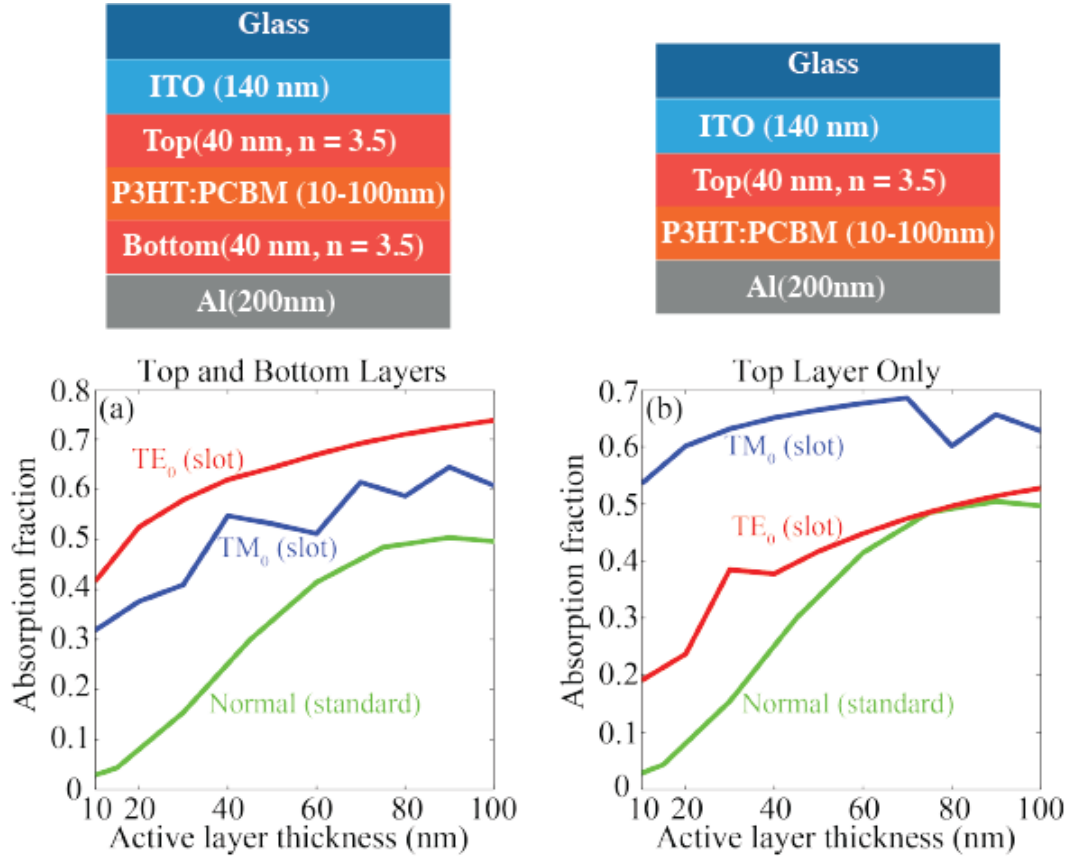
Figure 2.5.3: Absorption fraction, averaged over the AM1. 5G solar spectrum, of a slot OPV structure (glass/ITO/Top/$P3HT : PCBM$/ Bottom/Al) with: (a) $n_{Top}=n_{Bot}=3.5$, $k_{Top}=k_{Bot}=0$, and (b) $n_{Top}=3.5$, $k_{Top}=0$, and no Bottom layer. "TE_0 (slot) " and "TM_0 (slot)" refer to the guided modes in a slot OPV. "Normal (standard)" refers to normal incidence on a standard OPV (glass/ITO/PEDOT:PSS/ $P3HT : PCBM$/Al). The active-layer thickness is given by the x-axis. All calculations assume the following layer thicknesses: t_{glass}=semi-infinite, t_{IT0}= 140 nm, t_{Top}=40 nm, t_{Bot}=40 nm, t_{Al}=200 nm.

layers with thicknesses approaching the exciton diffusion length in these materials. Comparing this result to the guided-mode absorption for a standard OPV showed in Fig. 2.5.2(d), we see that the presence of the high-index Top and Bottom hole- and electron-transport layers adjacent to the active layer in the slot OPV case improves the absorption of the TM_0 and TE_0 modes in ultrathin active layers, with the improvement in the TE_0 mode being most pronounced. This may prove especially important from a practical perspective since the selective coupling of incident sunlight into TM modes is certainly less efficient than coupling into either TM or TE guided modes, as the slot OPV design allows.

From Fig. 2.5.3(b), we see that removal of the Bottom layer between the $P3HT$:PCBM and Al layers improves the absorption fraction of the TM_0 mode, but decreases that of the TE_0 mode. Specifically, the absorption of the guided modes in a slot OPV is equal to the "Normal (standard)" ($t_{active} = 100$ nm) absorption fraction of about 0.5 for a slot OPV active-layer thickness of (<10 nm, 90 nm) for the (TM_0, TE_0) modes, respectively. Figs. 2.5.3(a) and (b) demonstrate that is possible to equal or exceed the absorption of normally incident light on a "Normal (standard)" ($t_{active} = 100$ nm) cell with guided-mode absorption in an ultrathin "slot OPV".

The behavior observed in Fig. 2.5.3 can be understood by looking at Fig. 2.5.4, which plots the distribution of the square of the electric-field magnitude ($|E|^2$) for TE_0 (red) and TM_0 (TM1 for Fig. 2.5.4(a)) (blue) modes at A = 500 nm throughout a 10 nm-thick-active-layer slot OPV

28

device. Fig. 2.5.4 considers a slot OPV with the structure: glass

(semi-infinite, not shown) / ITO (140 nm) / Top (40 nm) / $P3HT : PCBM$

(10 nm) / Bottom (40 nm) / Al (200 nm), for the case of: (a)

$n_{Top} = n_{Bot} = 3.5$; (b) $n_{Top} = 3.5$, No Bottom layer, (c)

$n_{Top} = 1.8$, $n_{Bot} = 1.8$, and (d) $n_{Top} = 1.8$, No Bottom layer, with $k_{top} = k_{bot}$

$= 0$ for all panels (a)-(d). The maximum value of $|E|^2$ for each plotted mode

is normalized to 1. When one is using Fig. 2.5.4 ($|E|^2$) to help understand

the results of Fig. 2.5.3 (absorption fraction in the active layer), it is

important to remember that the absorption fraction of the active layer

depends on electric field distribution in the layers, as well as the absorption

strength of the active layer relative to other layers in the structure.

Fig. 2.5.4(a) shows that for $n_{Top} = n_{Bot} = 3.5$ the TE_0 mode is mostly

confined near the active layer, and due to the "slot-waveguide" effect, the

TM_0 mode is tightly confined in the active layer [1]. This leads to strong

absorption in active layer for both modes. As Fig. 2.5.4(b) shows, removing

the Bottom Layer shifts the TE_0 mode away from the active layer and

toward the Top layer, resulting in lower absorption than for the

Top-and-Bottom-layer case in Fig. 2.5.4(a). This can also be seen by

comparing the TE_0 mode absorption shown in Fig. 2.5.3(b) with that shown

in Fig. 2.5.3(a). However, for the TM_0 mode in Fig. 2.5.4(b), we can see

that removing the Bottom Layer leads to stronger active-layer confinement

and stronger absorption than the Top-and-Bottom-layer case in Fig. 2.5.4(a).

This can also be seen by comparing the TM_0 mode absorption shown in Fig.

2.5.3(b) with that shown in Fig. 2.5.3(a). The ideal configuration for a given
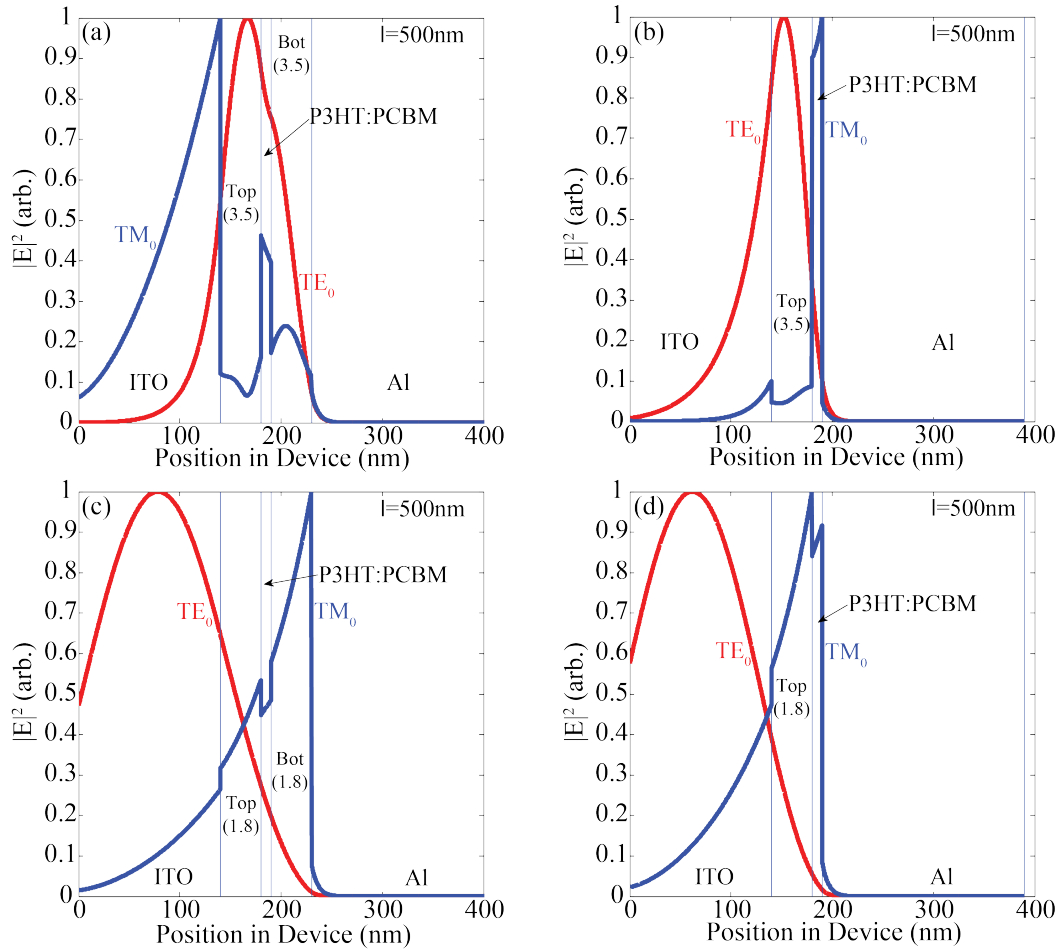
Figure 2.5.4: Distribution of the electric field magnitude squared ($|E|^2$) at $\lambda = 500\,\text{nm}$ throughout a 10 nm-thick-active-layer slot OPV device-glass (semi-infinite, not shown) / ITO (140 nm) / Top (40 nm) / $P3HT : PCBM$ (10 nm) / Bottom (40 nm) / Al (200 nm) - for the case of: (a) $n_{\text{Top}} = n_{\text{Bot}} = 3.5$; (b) $n_{\text{Top}} = 3.5$, No Bottom layer, (C) $n_{\text{Top}} = 1.8, n_{\text{Bot}} = 1.8$, (d) n_{Top}=1.8, No Bottom layer. $k_{Top}= k_{Bot}$=0 for all panels (a)-(d). Line colors are: Red=TE_0 guided mode, and Blue=TM_0 guided mode. Vertical lines show the separation between different layers in the cell. The maximum value of $|E|^2$ for each plotted mode is normalized to 1.

application will depend on many factors, including the ability to couple selectively into specific modes such as TM_0, in which case a Top-Layer-Only design may be desired.

Figs. 2.5.4(c) and (d) consider the cases of low-index Top and Bottom layers: (c) $n_{Top} = 1.8$, $n_{Bot} = 1.8$. and (d) $n_{Top} = 1.8$, No Bottom layer, allowing us to understand the effect of reducing the real part of the refractive index. For the TE_0 mode, as the real parts of the refractive indices of the Top and Bottom layers decrease, the peak of the mode moves from the Top layer towards the ITO layer, resulting in decreased field amplitude in the active layer. For the TM_0 mode, as the real parts of the refractive indices of the Top and Bottom layers decrease, the confinement in the active layer weakens and even reverses. From this comparison, it is clear that the practical realization of ultrathin OPVs with improved power conversion efficiency will require high-index layers on either side of the active layer to enable sufficient optical confinement in the active layer. These high index layers may take the form of hole- and electron-transport layers as shown in Fig. 2.5.3(a), or a transport layer on one side and a metal electrode on the other side as shown in Fig. 2.5.3(b).

Theoretical investigations from previous works have studied the ultimate limit of guided-mode absorption in slot-waveguide devices [7, 59]. The local density of optical states (LDOS) within the low index slot will be increased due to the presence of the high index cladding layers, which have an LDOS significantly higher than that for a bulk slab of the low index materials [7]. While both theoretical and computational have shown that the

31

slot OPV structure will enhance the light absorption in the active layer, in the actual implementation, the need for high index layers make the efficient coupling of incident sunlight into the guided modes more difficult due to the reflection from high index material.

The actual materials we may use for the top and bottom layer is $TiO_2(n = 2.6)$ and $V_2O_5(n = 2.3)$. The simulation result is shown in Fig. 2.5.5 We see that the absorption fractions of the guided modes in this case are equal to the $t_{active} = 100$ nm absorption fraction of about 0.5 for the "Normal (standard)" case for a slot OPV active-layer thickness of (60 nm, 45 nm) for the (TM_0, TE_0) modes, respectively.

2.5.3 Experimental way to measure Effective indices of the guided mode

We use a prism coupler (Metricon Model 2010) to measure the effective indices of the guided modes in a sample, as shown in Fig. 2.5.6[16, 54, 71, 76]. This setup consists of a prism that is contacted to the thin film sample, with the air gap (typically measuring around 100 nm) between the prism and sample controlled via the pressure in a pneumatic coupling head that pushes the sample into the face of the prism. A pressure of 45 psi is typically used, yielding an air gap of about 100 nm. In order to make sure this pressure does not deform the film under study, we tune the incident angle of the laser on the prism to coincide with a guided mode (indicated by a dip in the intensity of the light reflected by the prism as measured by the photodetector) and verify that as the pressure is swept over a range (30 psi – 55 psi) centered on
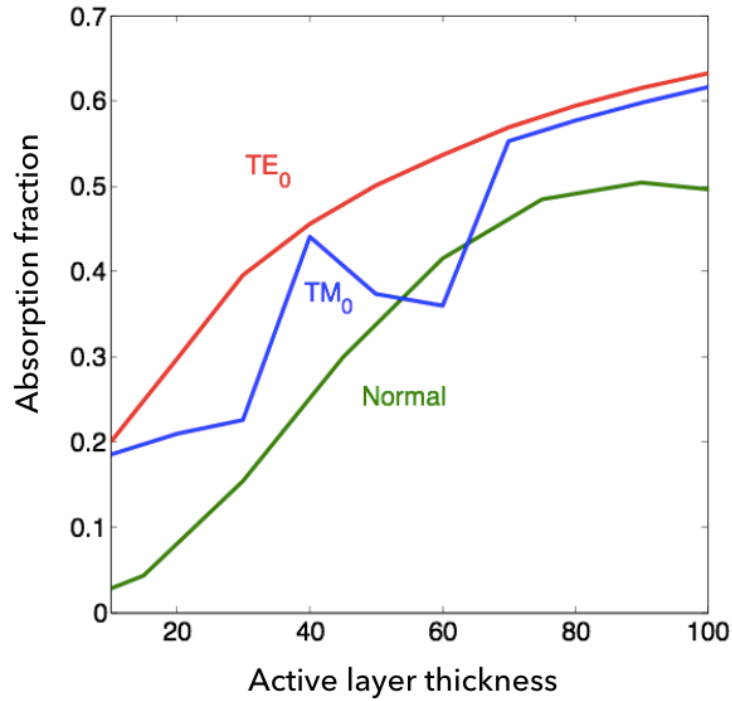
Figure 2.5.5: Absorption fraction, averaged over the AM1. 5G solar spectrum, of a slot OPV structure with real top and bottom materials (glass / ITO / TiO_2 / $P3HT : PCBM$ / V_2O_5/Au) with: $n_{Top} = 2.6$ n_{Bot}=2.3, k_{Top}=k_{Bot}=0. "TE_0 (slot) " and "TM_0 (slot) " refer to the guided modes in a slot OPV. "Normal (standard)" refers to normal incidence on a standard OPV (glass/ITO/PEDOT:PSS/ $P3HT : PCBM$/Al). The active-layer thickness is given by the x-axis. All calculations assume the following layer thicknesses: t_{glass}=semi-infinite, t_{IT0}= 140 nm, t_{Top}=40 nm, t_{Bot}=40 nm, t_{Au}=9 nm.

the pressure used in the experiment (45 psi), the incident laser angle at which the dip occurs remains unchanged. The fact that the angle remains unchanged as the pressure is varied indicates that over the measured range of angles, the thickness of the film does not vary significantly. As the laser angle is swept, the light undergoes total internal reflection within the prism and the photodetector measures the intensity of the reflected light. When the phase velocity of the incident light of the sample / prism interface component is equivalent to the phase velocity of a guided mode, resonant energy transfer occurs from the incident light into the structure via "optical tunneling" [79]. For the setup shown in Fig. 2.5.6, we detect the reflected optical intensity as the laser angle (and therefore the incident phase velocity) is scanned, resulting in intensity minima measured by the detector at angles that allow resonant coupling to the guided modes of the sample. The position of these minima determine the effective indices of the guided modes, which are the propagation constants (divided by the vacuum wavevector) of the electromagnetic wave within the plane of the thin film.

Fig. 2.5.7 shows the comparison of the prism coupler measurement result and the FDTD simulation result for the structure glass(700um) / ITO(140nm) / TiO_2 (30nm) / P3HT:PCBM (98nm) / V_2O_5 (40nm) / Au (9nm) with the prism contacting the Au side of the cell. The experimentally measured ($\beta_{TE_0} = 1.85$ and $\beta_{TM_0} = 1.67$) and the numerically calculated ($\beta_{TE_0} = 1.84$ and $\beta_{TM_0} = 1.70$) mode positions are in good agreement [16].
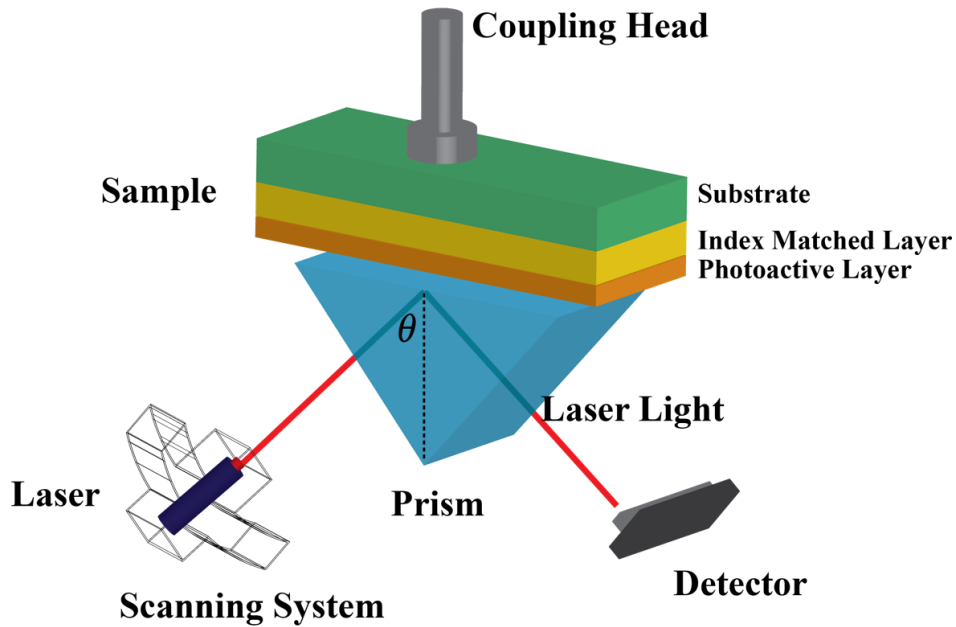
Figure 2.5.6: Prism coupler setup used to measure the effective indices of the sample.

2.6 SUMMARY AND OUTLOOK

We introduced a novel OPV design, termed a "slot OPV", that applies the principles of slot waveguides to tightly confine light within the active layer of an ultrathin OPV structure. Our calculations demonstrated that by judicious design of the layers and their optical properties, a "slot OPV" can be designed with a guided-mode absorption fraction for a 10 nm thick active layer that is equal to the absorption fraction of normal incidence on a "Standard OPV" with 100 nm thick active layer. These results, together with the expected improvement in charge extraction for ultrathin layers, suggest that ultrathin OPVs can be designed with greater overall power conversion efficiency than today's state-of-the-art OPV architectures if we
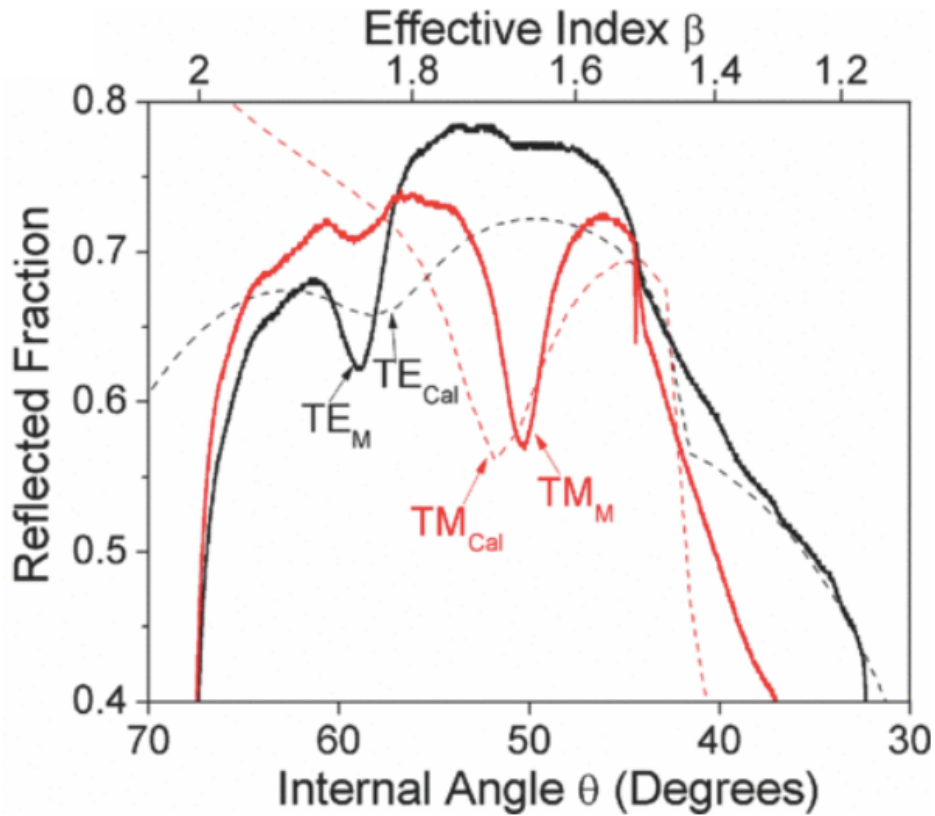
Figure 2.5.7: Comparison of the prism coupler measurement result and FDTD simulation result [16]. The structure for the measurement and simulation is glass(700um) / ITO(140nm) / TiO_2 (30nm) / P3HT:PCBM (98nm) / V_2O_5 (40nm) / Au (9nm). Solid lines: Fraction of incident TE (black, denoted TE_M) and TM (red, denoted TM_M) polarized 633 nm laser reflected from the prism-device interface and detected by the detector as shown in Fig. 2.5.6. Dashed lines: Same quantity calculated using Lumerical FDTD for the TE(black, denoted as TE_{Cal}) and TM (red, denoted as TM_{Cal}) polarizations.

can couple the incidence light into the specific guided modes. For instance, the absorption fraction for TE_0 guided mode within a 10nm active layer is around four times better in our slot OPV design than the typical OPV architecture.

In this chapter, we are assuming that there is no variation of material properties throughout the depth of the photoactive layer. In real practice, the performance of many thin-film photovoltaics (PV) is significantly influenced by the variation of material properties throughout the depth of the photoactive layer. The accurate measurement of the resulting "depth profiles" for optical and electronic properties such as refractive index and charge collection probability is critical to the understanding, modeling and optimization of these devices. In Chapters. 3 - 7, we will describe several methods to measure and reconstruct the "depth profiles" for both optical(refractive index) and electronic properties (charge collection probability).

CHAPTER 3

RECONSTRUCTING THE CHARGE COLLECTION PROBABILITY FROM THE PROBABILITY DENSITY FUNCTION AND MEASUREMENT OF THE INTERNAL QUANTUM EFFICIENCY

3.1 INTRODUCTION

In this Chapter, we apply a new, non-destructive technique that was recently developed in our lab [15] to the accurate reconstruction of collection probability depth profiles within the $Cu(In, Ga)Se_2$ (CIGS) absorber layers. The charge collection probability $\phi(z)$ is defined as the probability that a carrier generated by light absorption at position z of the device will be collected and therefore contribute to the light-generated current. It mainly

38

depends on the distance that a light-generated carrier must travel compared to the diffusion length, but also dependent on the surface properties of the devices [28].

While the electron-beam-induced current (EBIC) method has been used in the past to successfully reconstruct the charge collection probability [17, 37, 43, 61], this approach is destructive and requires time-consuming sample preparation, it also change the charges state of defects within CIGS absorber layer, resulting in a change of $\phi(z)$ with electron energy [37], in violation of the assumption of the $\phi(z)$ is the same for all measurements. In this chapter, we described a novel optical and non-destructive method for the direct reconstruction of the charge collection probability $\phi(z)$ from the measurement of IQE as a function of wavelength ($\eta(\lambda)$). Our nondestructive optoelectronic method avoids the drawbacks from EBIC method, allows the bias voltage, bias light, and temperature to be easily varied, and also allows $\phi(z)$ to be reconstructed for a wider range of materials, including those which would be damaged by EBIC.

Below we first describe the mathematical basis of our approach, and then apply it to a computational example that assumes a charge collection probability $\phi(z)$ of a "canonical" CIGS system to demonstrate the method's accuracy. Finally, we apply this method to IQE data measured on a CIGS solar cell.
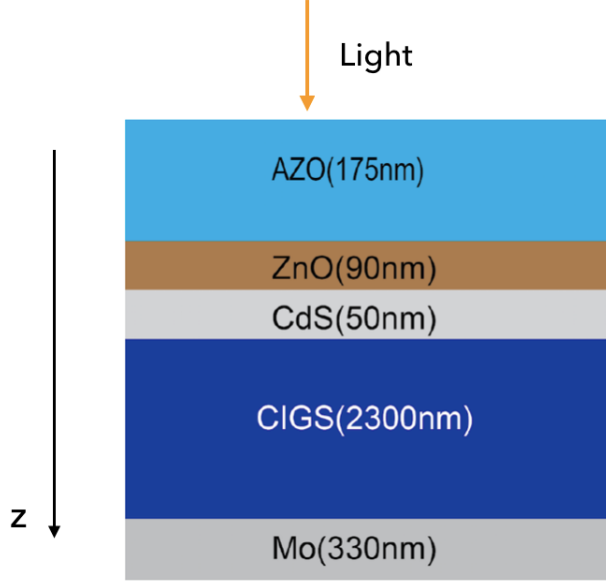
Figure 3.2.1: Generic schematic of an CIGS solar cell. With structure:Mo (330nm)/CIGS(2300nm)/CdS(50nm)/ZnO(90nm)/AZO(175nm).

3.2 STATEMENT OF THE PROBLEM

Letting $G(z, \lambda)$ be the normalized probability distribution per unit length of creating an electron-hole pair at depth z for the laser wavelength λ, the basic relation between the depth-dependent charge-collection probability $\phi(z)$ within the device and the externally measured IQE ($\eta(\lambda)$) is

$$\eta(\lambda) = \int\limits_{0}^{t_{CIGS}} G(z, \lambda)\phi(z)dz \tag{3.1}$$

where t_{CIGS} is the thickness of the CIGS absorber layer and $G(z, \lambda) = 0$ for $z < 0$ and $z > t_{CIGS}$. $G(z, \lambda)$ can be calculated from the electric field distribution throughout the device once we know the thickness
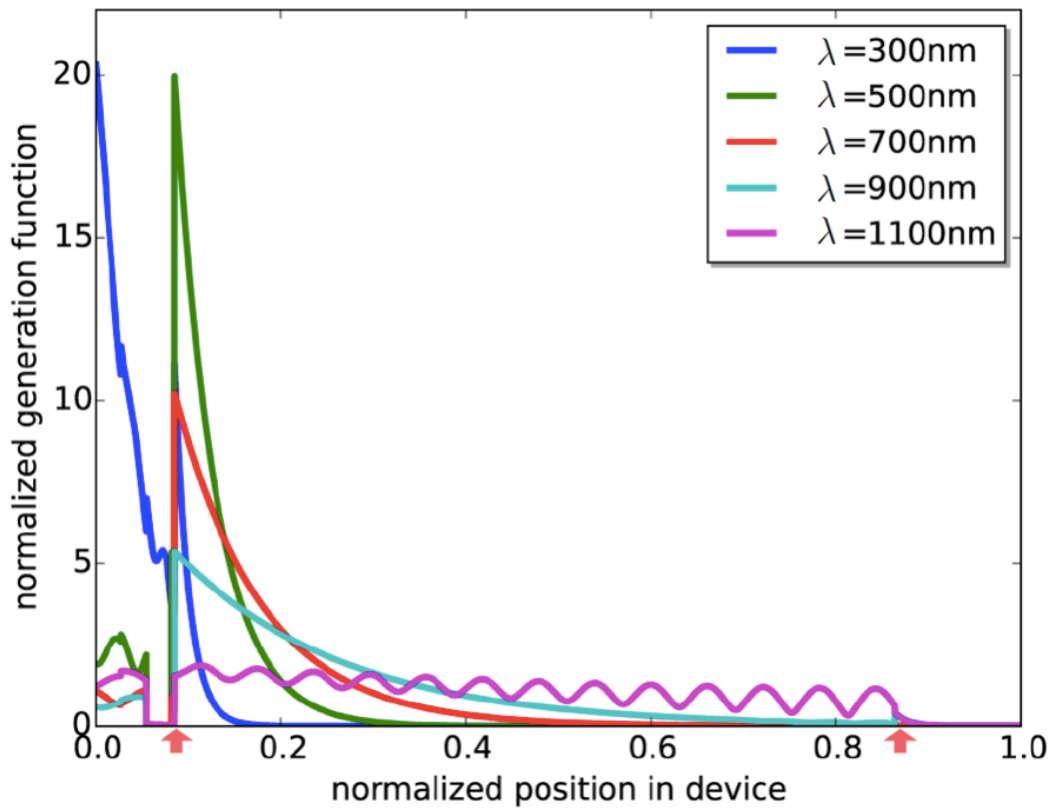
Figure 3.2.2: The normalized probability density function, $G(z, \lambda)$ for CIGS solar cell with the structure shown in Fig. 3.2.1, the red arrows indicate the start and end of the CIGS absorber layer.

and refractive index of each layer as shown in Fig. 3.2.1. Fig. 3.2.2 shows the plot of $G(z, \lambda)$ for the CIGS solar cell with the structure shown in Fig. 3.2.1, as calculated using the Finite Difference Time Domain (FDTD) method with the Lumerical refractive index database. After, we measured $\eta(\lambda)$ for different wavelengths, $\phi(z)$ are obtained by using Eq. 3.1 above to find the best-fit parameters in the following parametrized functional forms [37]:

when $0 \leq z < z_{SCR}$

$$\varphi(z) = 1 \tag{3.2}$$

when $z_{SCR} \leq z \leq z_{Mo}$ (neutral bulk region)

$$\varphi(z) = \frac{\left(\frac{1}{L_{eff}} \cosh\left[\frac{z-z_{Mo}}{L_{eff}}\right] - \frac{S_{Mo}}{D} \sinh\left[\frac{z-z_{Mo}}{L_{eff}}\right]\right)}{\frac{1}{L_{eff}} \cosh\left[\frac{z_{Mo}-z_{SCR}}{L_{eff}}\right] + \frac{S_{Mo}}{D} \sinh\left[\frac{z_{Mo}-z_{SCR}}{L_{eff}}\right]} \tag{3.3}$$

where z_{Mo} represents the Position of CIGS/Mo interface, z_{SCR} represents the depth of space-charge region, L_{eff} represents minority carrier diffusion length, S_{Mo} represents the recombination velocity at CIGS/Mo and D represents diffusion constant. The collection probability within the neutral bulk region is derived using reciprocity theorem with boundary conditions at the space-charge region and the CIGS/Mo interface [58]. To calculate charge collection probability $\phi(z)$, a least-squares fit to measured $\eta(\lambda)$ values is carried out via Eq. 3.1 using calculated $G(z, \lambda)$ distributions.

3.3 Least-squares fit with Gradient decent

In order to demonstrate the benefits and reliability of our methods, We consider the structure:Mo(330nm) / CIGS(2300nm) / CdS(50nm) /

ZnO(90nm) / AZO(175nm) shown in Fig. 3.2.1, and a simulated charge collection probability $\phi(z)$ shown in Eq. 3.2 and Eq. 3.3, where $z_{m0} = 2300nm$, $z_{SCR} = 350nm$, $L_{eff} = 900nm$ and $S_{Mo}/D = 4 \times 10^3 cm^{-1}$. By substituting this ϕ and simulated $G(z, \lambda)$ into Eq. 3.1, we can obtain the simulated exact values of $\eta(\lambda)$. This was done for N = 81 values of λ equally space between 300nm and 1100nm.

Assuming that in Eq. 3.3, we have two unknown parameters x_1: L_{eff} and x_2: S_{Mo}/D. We can use least-squares fit with gradient decent to find the best values for x_1 and x_2 with Eq. 3.1 [46]. The least-squares cost function is shown as the following format:

$$J(x_1, x_2) = \sum_\lambda \left[\int_0^{t_{CIGS}} G(z, \lambda)\varphi(z, x_1, x_2)dz - \eta(\lambda) \right]^2 \qquad (3.4)$$

Fig 3.3.1 shows the least-squares cost function of the parameters x1: L_{eff} and x2: S_{Mo}/D. The color-bar shows the value of the $\log_2(F(x_1, x_2))$. In order to find the x_1, x_2 that minimize the cost function, we use gradient decent algorithm as the following steps:

- Start with $x_1 = 890nm$, $x_2 = 4.1 \times 10^3 cm^{-1}$ (can be initialized with other values).

- Repeat this step until convergence:

$$x_j = x_j - \alpha \frac{\partial}{\partial x_j} J(x_1, x_2) \quad for \ j = 1 \ \ and \ j = 2$$

$x_1 = 899.980nm$, $x_2 = 3.997 \times 10^3 cm^{-1}$ after 20 iteration.
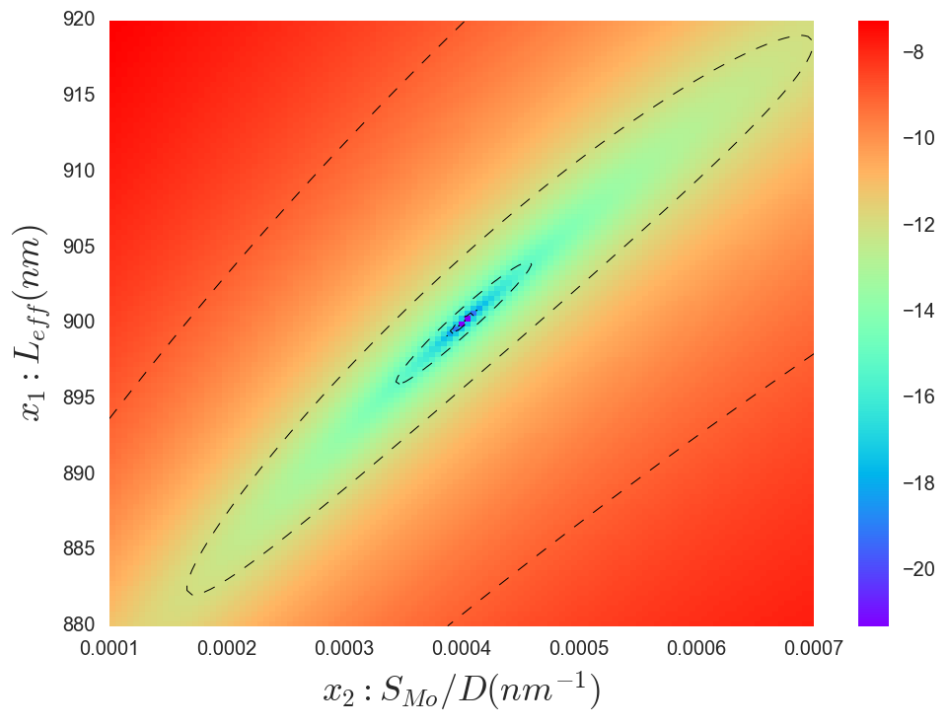
Figure 3.3.1: Least-sqaures cost function of the parameters x1: L_{eff} and x2: S_{Mo}/D. The color-bar shows the value of the $\log_2(J(x_1, x_2))$

3.4 EXPERIMENTAL RESULTS AND DISCUSSION

In this section, we apply the method to IQE measured on an actual CIGS solar cell at 81 equally spaced wavelength between 300nm and 1100nm with the structure shown in Fig. 3.2.1. We obtain the reconstruction of the charge collection probability $\phi(z)$ as shown in Fig 3.4.1 with $z_{m0} = 2300nm$ (fixed), $z_{SCR} = 350nm$ (measured via capacitance-voltage), $L_{eff} = 920nm$ and $S_{Mo}/D = 4.3 \times 10^3 cm^{-1}$.

Finally, we substitute the reconstructed charge collection probability $\phi(z)$ and the normalized probability G back to Eq. 3.1 to obtain the calculate IQE shown in the Fig. 3.4.2 as the blue stars.

The errors of the reconstruction come from two primary sources:

- It is a model and parameter dependent method, which means we need to know the true form of the charge collection probability model beforehand. Any deviation from the model will lead to error in the reconstruction.

- In this work, we assuming that there is no variation of the refractive index throughout the depth of the CIGS active layer. In real practice, the refractive index profile is significantly influenced by the variation of material properties throughout the depth of the CIGS photoactive layer [47]. The accurate measurement of the resulting "depth profiles" is critical to the modeling of the $G(z, \lambda)$ distributions.

To improve the fit, in Chapters 4 and 5, we developed a novel
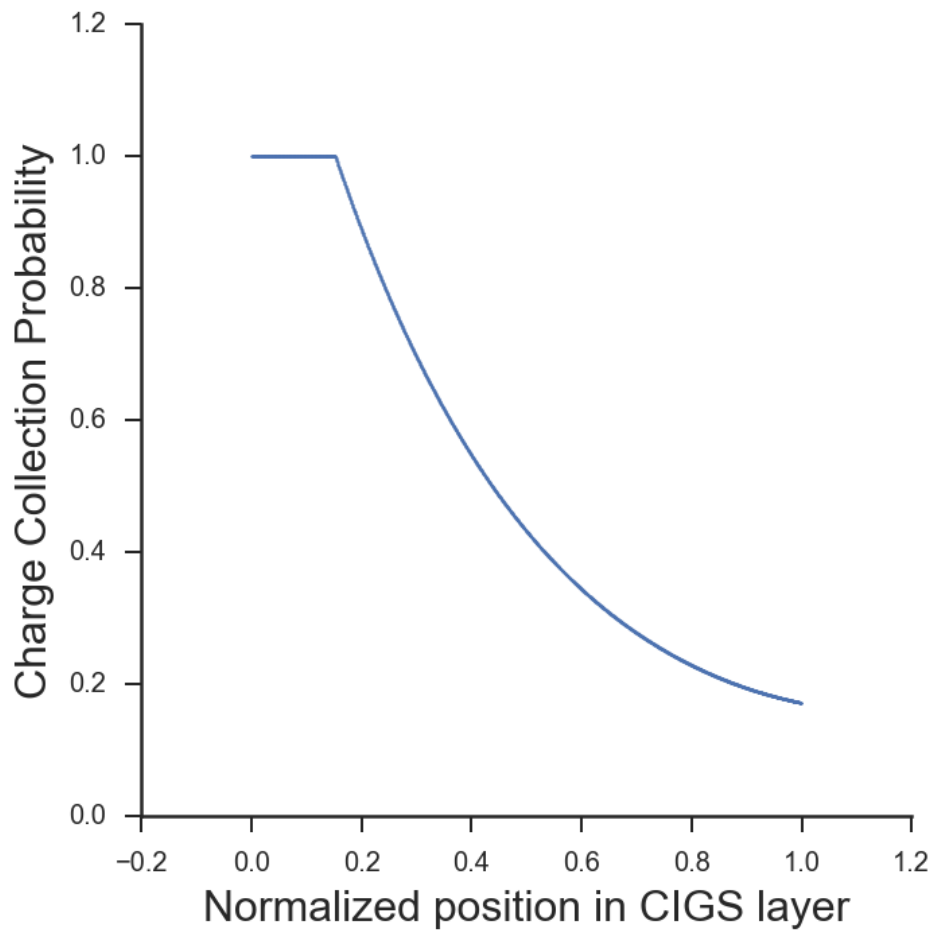
Figure 3.4.1: Reconstruction of the charge collection probability data point in the CIGS layer from the IQE measurements using Least-squares fit with Gradient decent method.
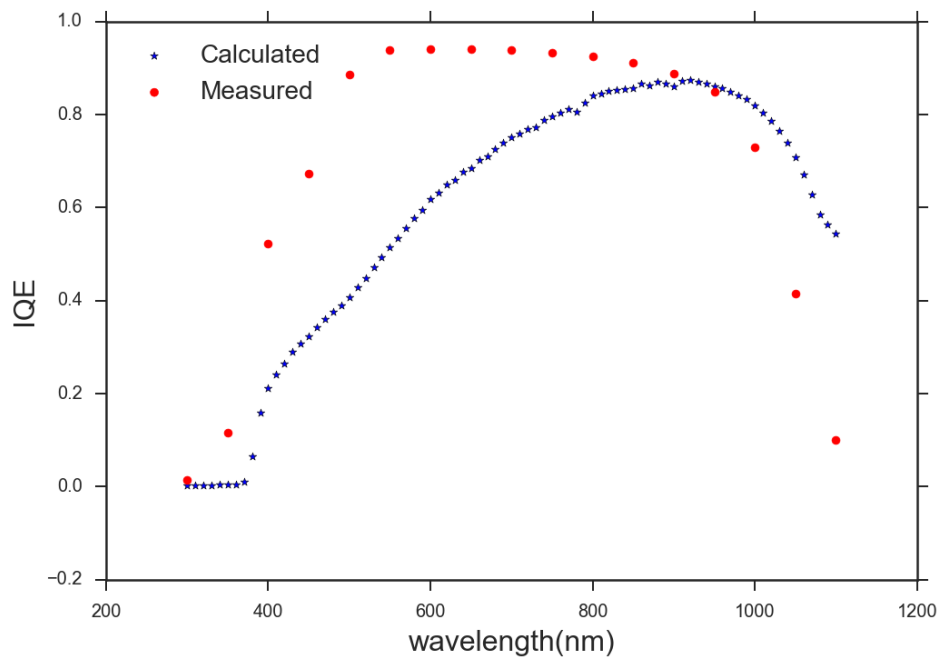
Figure 3.4.2: Measured and Calculated IQE for the CIGS solar cell. The blue stars represents the calculated IQE from the reconstruction of the charge collection probability and the red point represent the measured IQE.

nondestructive and parameter-independent optoelectronic method for the reconstruction of the charge collection probability profiles within CIGS solar cells. In Chapters 6 and 7, we demonstrated a new method for reconstructing the depth-dependent refractive-index profile in thin films with high spatial resolution.

3.5 Summary And Outlook

In summary, we have developed a novel nondestructive optoelectronic method for the reconstruction of the charge collection probability profiles within CIGS solar cells.

Although we focused on the application of this technique to CIGS solar cells in this Chapter, this method also applies to other types of solar cells [15].

Part II

New Reconstruction Techniques

for improved model accuracy

CHAPTER 4

RECONSTRUCTING THE CHARGE COLLECTION PROBABILITY USING THE REGULARIZATION METHOD

4.1 INTRODUCTION

This Chapter contributes to the understanding of the charge collection probability $\phi(z)$ in thin-film solar cells with polycrystalline $Cu(In, Ga)Se_2$ (CIGS) absorber layers. In this work, we described a novel optical, non-destructive and parameter-independent method for the direct reconstruction of the charge collection probability $\phi(z)$ from the measurement of IQE as a function of wavelength $(\eta(\lambda))$. This inversion process is an ill-posed problem, but a stable solution can be found by applying the regularization method.

Below we first describe the mathematical basis of our approach, and then apply it to a computational example that assumes a charge collection

probability $\phi(z)$ of a "canonical" CIGS system to demonstrate the method's accuracy. Finally, we apply this method to IQE data measured on a CIGS solar cell.

4.2 STATEMENT OF THE PROBLEM

Eq. 3.1 is a special instance of the Fredholm integral equation, with the kernel given by $G(z, \lambda)$. $G(z, \lambda)$ can be calculated from the electric field distribution throughout the device once we know the thickness and refractive index of each layer as shown in Fig. 3.2.1. Fig. 3.2.2 shows the plot of $G(z, \lambda)$ for the CIGS solar cell with the structure shown in Fig. 3.2.1, as calculated using the Finite Difference Time Domain (FDTD) method with the Lumerical refractive index database.

The first step to obtain a numerical solution of Eq. 3.1 is to change the integral equation to matrix form by applying the midpoint discretization method [63]. Suppose that $\eta(\lambda)$ has been measured for selected wavelength values $\lambda_i, i = 1, ...N$; Let $\eta_i = \eta(\lambda_i)$. A simple way of discretizing Eq. 3.1 is using quadrature methods [51]. We assume that $\phi(z)$ is a piecewise constant function, having the value ϕ_j in the interval (t_{j-1}, t_j), where $t_0 = 0$ corresponds to the start of the CIGS layer (Here we assume the charge collection probability is 0 outside the CIGS active layer). After the discretization, Eq. 3.1 becomes

$$\eta_i = \sum_{j=1}^{N} G_{ij}\phi_j \quad i = 1, \ldots, N \tag{4.1}$$

with

$$G_{ij} = \int_{t_{j-1}}^{t_i} G(z, \ \lambda_i)dz \tag{4.2}$$

It is known that linear systems arising from the first kind Fredholm integral equation such as Eq. 3.1 are likely to be ill-conditioned [51].

4.3 SINGULAR VALUE DECOMPOSITION (SVD) ANALYSIS AND THE PICARD CONDITION

The singular value decomposition (SVD) is a very powerful tool for analyzing first kind Fredholm integral equation [74].

In our cases, the matrix $G \in R^{N \times N}$ in Eq. 4.1 is square, and therefore the SVD of G takes the form

$$G = U\Sigma V^T = \sum_{i=1}^{N} u_i \sigma_i v_i^T \tag{4.3}$$

where $\sum \in R^{N \times N}$ is a diagonal matrix with the singular values, satisfying

$$\sum = diag(\sigma_1, \ldots, \sigma_n), \quad \sigma_1 \geq \sigma_2 \geq \cdots \geq \sigma_n \geq 0 \tag{4.4}$$

The matrix $U \in R^{N \times N}$ and $V \in R^{N \times N}$ consist of the left and right singular vectors

$$U = (u_1, \ \ldots, \ u_N), \quad V = (v_1, \ \ldots, \ v_N) \tag{4.5}$$

After we have performed SVD on the matrix G, the solution of ϕ in Eq.

4.1is given by

$$\phi = G^{-1}\eta = \sum_{i=1}^{N} \frac{u_i^T \eta}{\sigma_i} v_i \qquad (4.6)$$

For a stable solution ϕ to exist, the right-hand side coefficients $u_i^T \eta$ must decay to zero faster than the singular values σ_i, a situation that is referred to as the Picard condition. The violation of the Picard condition is the simple explanation of the instability of the inverse problem in the form of a first-kind Fredholm integral equation, but it also gives a way to deal with the ill-posed problem, by employing the truncated SVD regularization method.

4.4   TRUNCATED SVD REGULARIZATION METHOD

From the discussion in the previous section, we compute a regularized approximate solution by simply eliminating those SVD components where the $u_i^T \eta$ decay to zero more slowly than the singular values σ_i. Hence, we define the truncated SVD (TSVD) solution ϕ_k as the solution obtained by:

$$\phi_k = \sum_{i=1}^{k} \frac{u_i^T \eta}{\sigma_i} v_i \qquad (4.7)$$

The truncation parameter k should be chosen such that all the noise-dominated SVD coefficients ($u_i^T \eta$ terms that decay to zero more slowly than the singular values σ_i) are discarded. The value of k can be found from an inspection of the Picard plot as shown in Fig. 4.5.1.
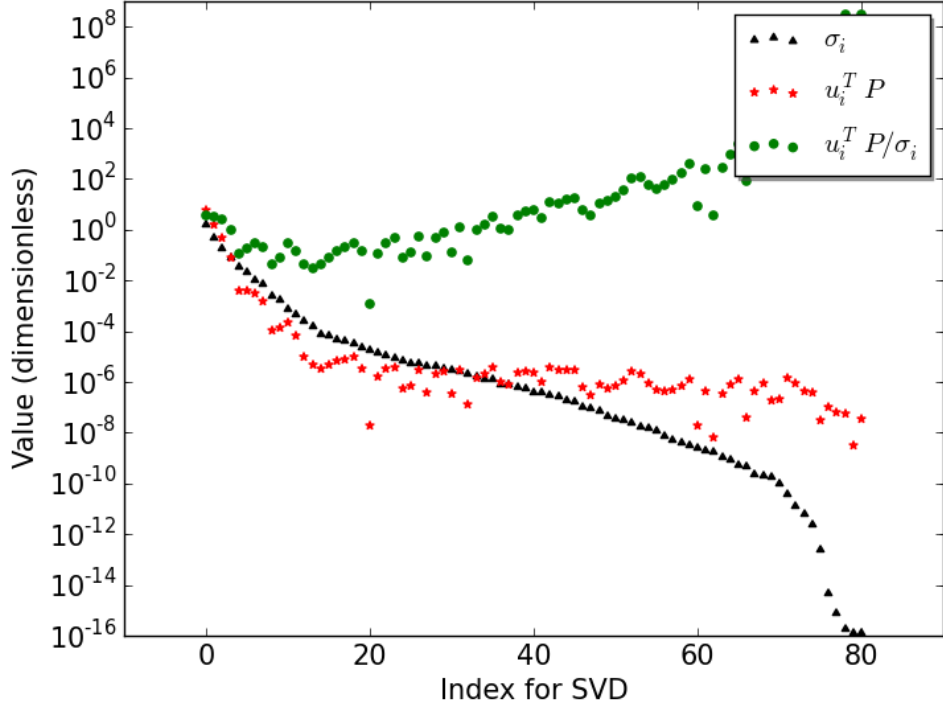
Figure 4.5.1: The Picard Plot for the charge collection probability reconstruction problem.

4.5 NUMERICAL RESULTS AND DISCUSSION

In order to demonstrate the benefits and reliability of our methods, we first use FDTD calculations [54, 56] to simulate a sample structure with a known refractive index and thickness of each layer for the normalized probability density function $G(z, \lambda)$. We consider the structure: Mo (330nm) / CIGS(2300nm) / CdS(50nm) / ZnO(90nm) / AZO(175nm) shown in Fig. 3.2.1.

We tested this approach on a simulated charge collection probability

54

$\phi(z)$, where $0 < z < t_{CIGS}$, and t_{CIGS} is the thickness of CIGS layer. The usual assumption for $\phi(z)$ in the CIGS layer is $\phi(z) = 1$ for $0 < z < z_{SCR}$, where z_{SCR} is the depth of space-charge region, and $\phi(z) = exp[-(z - z_{SCR})/L]$, where L is the minority-carrier diffusion length. By substituting this ϕ and simulated $G(z, \lambda)$ into Eq. 3.1 (we assume that the charge collection probability is 0 outside the CIGS active layer), we can obtain the simulated exact values of $\eta(\lambda)$. This was done for N=81 values of λ equally space between 300nm and 1100nm.

To find the value of truncation parameter k in Eq. 4.7, we investigate the behavior of the SVD coefficients $u_i^T \eta$ and $u_i^T \eta / \sigma_i$ in Eq. 4.6. A plot of these coefficients, together with the singular values, is referred to as a Picard plot shown in Fig. 4.5.1. From this plot, we would choose k=17.

Fig. 4.5.2 is the plot of the assumed exact $\phi(z)$ and the N=81 simulated data points with k=17 in Eq. 4.7 which shows a good agreement between the exact assumed profile (solid red line) and the data points calculated using our method (black dots).

4.6 Experimental results and discussion

In this section, we apply the method to IQE measured on an actual CIGS solar cell at 81 equally spaced wavelength between 300nm and 1100nm with the structure: Mo (330nm) / CIGS(2300nm) / CdS(50nm) / ZnO(90nm) / AZO(175nm) shown in Fig. 3.2.1. From the Picard Plot shown in Fig. 4.6.1, we choose the truncation parameter k = 4. With the the
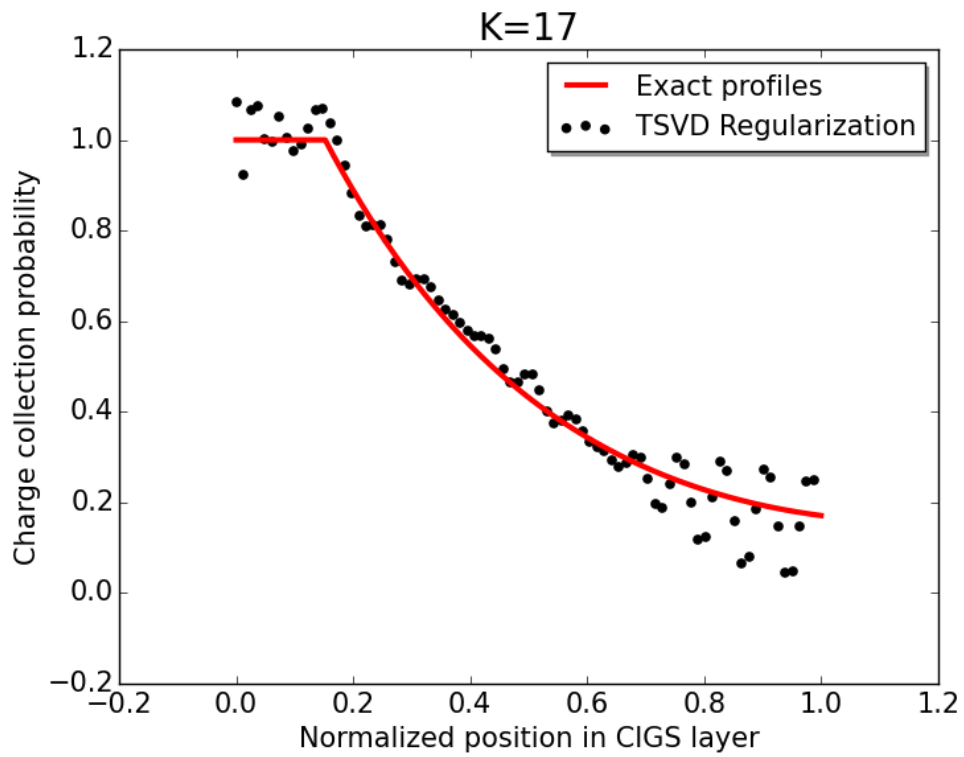
Figure 4.5.2: Typical simulated charge collection probability data in the CIGS layer. The red line represents the assumed exact profile of ϕ and the black dots represent the simulated data points with k $=17$ in Eq. 4.7

normalized probability G^{-1} simulated from the known structure, the measured IQE $\eta(\lambda)$ and the truncation parameter k = 4, using Eq. 4.7 and Eq. 4.6, we can obtain the reconstruction of the charge collection probability ϕ as shown in Fig. 4.6.2.

Finally, we substitute the reconstructed charge collection probability ϕ and the normalized probability G back to Eq. 3.1 to obtain the calculated IQE shown in the Fig. 4.6.3 as the star points, which shows a good agreement with the measured IQE. However, from Fig. 4.6.2, we see that the reconstruction of the charge collection probability oscillates very rapidly at both the front and back interface, which is due to the small value of the truncation parameter. To increase the truncation parameter, we need a better device structure model that takes into account the surface roughness.

4.7 Summary and Outlook

In summary, we have developed a novel nondestructive and parameter-independent optoelectronic method for the reconstruction of the charge collection probability profiles within CIGS solar cells.

Application of the regularization technique to an ill-posed inverse problem is only possible if the data noise is within a specified range; the noise can come from both measurement and model. To solve an ill-posed inverse problem to which regularization cannot be applied due to noise, we introduce the Self-Constrained Ill-Posed Inverse Problem (SCIIP) method in
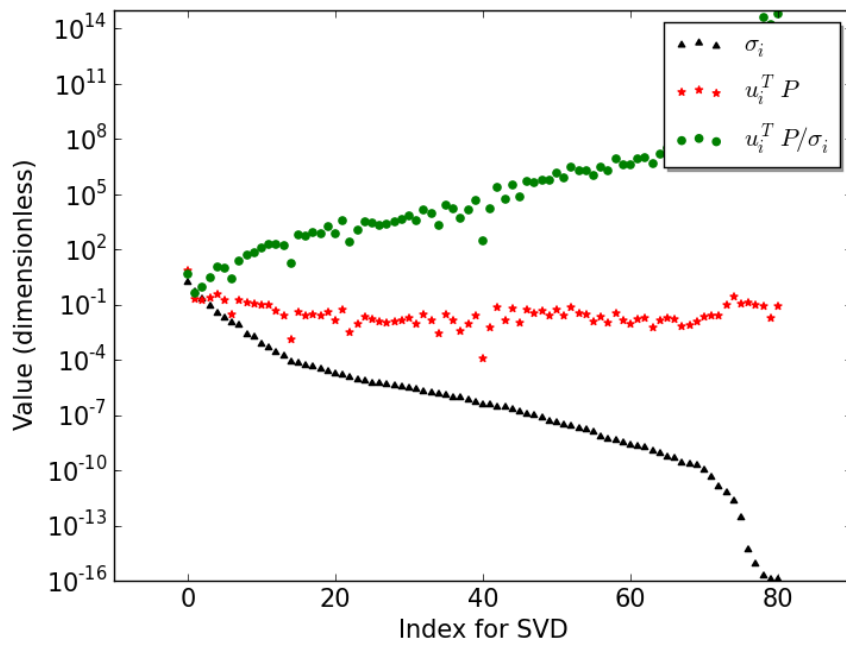
Figure 4.6.1: The Picard Plot for the charge collection probability reconstruction of the experiment.
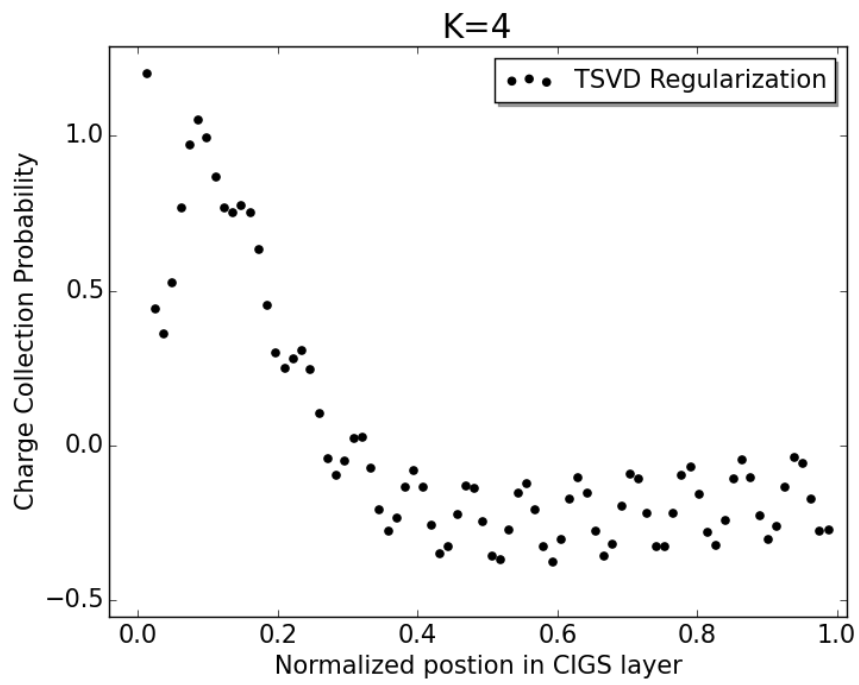
Figure 4.6.2: Reconstruction of the charge collection probability data points in the CIGS layer from the IQE measurements.
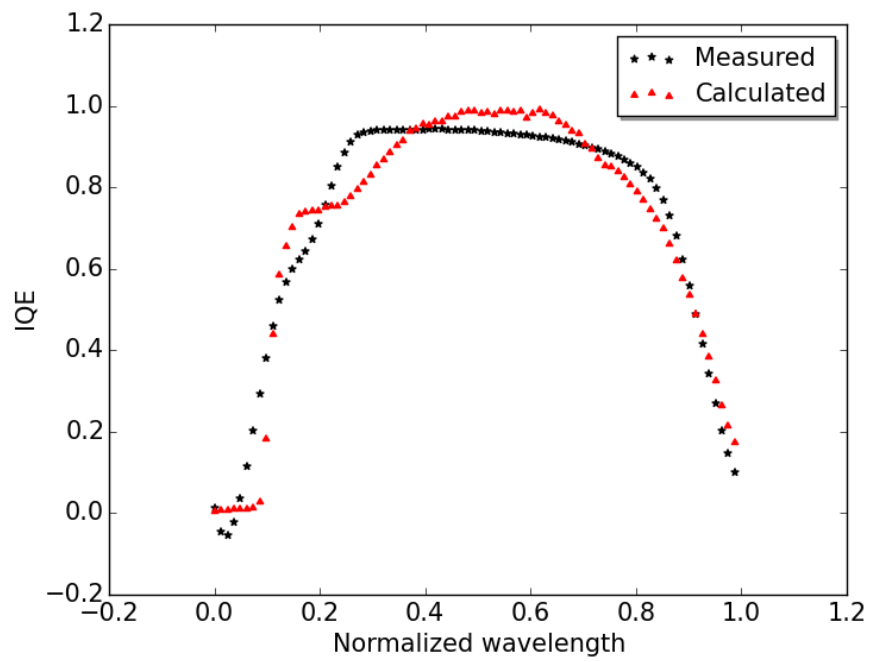
Figure 4.6.3: Measured and Calculated IQE for the CIGS solar cell. The black points represent the measured IQE, and the red points represent the calculated IQE from the reconstruction of the charge collection probability.

Chapter. 5. The SCIIP method improves the signal-to-noise of the solution by using the regularization method with system constraints and optimization via an evolutionary algorithm. With the SCIIP method, we can first search the data space within the noise range, pre-filter the noise, and then use it to find the regularization reconstruction result.

Although we focused on the application of this technique to CIGS solar cells in this chapter, this technique applies to inverse problems. In general in a wide range of fields, including subsurface mapping in geology [69], image reconstruction in astronomy or medicine [2, 14], and depth profiling of solar cells and other thin-film stacks [15, 55, 75], among others.

CHAPTER 5

SOLVING INVERSE PROBLEMS MORE AC-
CURATELY USING FEEDBACK

5.1 INTRODUCTION

Inverse problems, in which one reconstructs from a set of measurements, the source that produced the data comprising those measurements, are critical to a wide range of fields in science and mathematics, including subsurface mapping in geology [69], image reconstruction in astronomy or medicine [2, 14], and depth profiling of solar cells and other thin-film stacks [15, 55, 75], among others. Such problems are often ill-posed in that their solutions are highly sensitive to changes in the measurement results [69]. This poses a challenge to the solution of real-world inverse problems where measurement noise is unavoidable. To address this challenge, various regularization methods have been developed [19, 34, 72, 73], all of which allow the solution to ill-posed problems by

introducing additional constraints in some form. The discrepancy principle shows that we should choose the regularization parameter according to the noise level [27]. When the noise is very large, we are forced to choose large regularization parameters that can lead to under-fitting.

In this chapter, we introduce the Self-Constrained Ill-Posed Inverse Problem (SCIIP) method. Our method can improve the signal-to-noise even beyond the discrepancy principle, compared to the result obtained by applying standard regularization. Imagine that we have performed measurements, the results of which are denoted b, but we know that these measurements are composed of the actual quantity of interest plus noise. Our method relies on the fact that the actual quantity of interest without noise (denoted $b_{noiseless}$) must exist in the parameter space neighborhood of the measured result b_{meas}, and that $b_{noiseless}$ will give a better reconstruction (the smaller residual, the better) than b_{meas}. Our method searches the space $b \pm \eta$ (where η defines the search space, and should be on the order of the standard deviation of the noise to successfully find $b_{noiseless}$) using a Cellular Evolutionary Algorithm (CEA) to find the b that minimizes the residual. We then feed this new b into the regularization process, which yields a result x that is closer to the true x than would be obtained by just feeding b_{meas} directly into the regularization method.

5.2 Ill-posed inverse problem

This Chapter deals with one important class of linear inverse problems, which take the form of Fredholm integral equations of the first kind. A

Fredholm integral equation of the first kind is an integral equation of the form:

$$f(s) = \int_a^b K(s,t)\phi(t)dt \tag{5.1}$$

where $K(s,t)$ is the kernel and $\phi(t)$ is an unknown function for which we wish to solve.

The first step to obtaining a numerical solution of Eq. (5.1) is to change the integral equation to the matrix form by applying discretization method. In this work, we use the quadrature method to change the integral equation to the matrix form [25].

After the discretization, Eq. (5.1) becomes a linear system

$$Ax = b \tag{5.2}$$

The elements of the matrix A, the right-hand side b, and the solution vector x are given by

$$\left. \begin{array}{l} a_{ij} = \omega_j K(s_i, t_j) \\ x_j = \phi(t_j) \\ b_i = f(s_i) \end{array} \right\} \quad i,j = 1,...,n \tag{5.3}$$

It is known that linear systems arising from the first kind Fredholm integral equation such as Eq. (5.1) are likely to be ill-posed [51]. In order to solve the ill-posed inverse problem arising from the Fredholm integral equation, we need to use regularization method. In this Chapter, we will use Tikhonov Regularization method.

5.3 Tikhonov Regularization method

The Tikhonov solution x_λ is defined as the solution to the problem:

$$\min_x \left\{ \|Ax - b\|_2^2 + \lambda^2 \|x\|_2^2 \right\} \tag{5.4}$$

where, the first term $\|Ax - b\|_2^2$ measures the goodness-of-fit, and the second term $\|x\|_2^2$ measures the regulairty of the solution. The notation "$\|\vec{v}\|_2$" in Eq. (5.4) denotes the L2-norm of the vector $\vec{v}$:$\|\vec{v}\|_2 = \sqrt{\sum_{i=1}^n |v_i|^2}$. The balance between the two terms is controlled by the factor λ^2.

The solution of Eq. (5.4) can also be rewritten as follows in terms of the singular value decomposition (SVD) [27].

$$x_\lambda = \sum_{i=1}^n \phi_i^{[\lambda]} \frac{u_i^T b}{\sigma_i} v_i \tag{5.5}$$

where $\varphi_i^{[\lambda]}$ are the filter factors and take the form:

$$\varphi_i^{[\lambda]} = \frac{\sigma_i^2}{\sigma_i^2 + \lambda^2} \approx \begin{cases} 1 & \sigma_i \geq \lambda \\ \sigma_i^2/\lambda^2 & \sigma_i \leq \lambda \end{cases}$$

5.4 Discrepancy Principle

The regularization parameter λ is chosen by the discrepancy principle, which is described below.

For illustration, let's consider Tikhonov regularization, which has the

following properties.

- There exists a positive number δ_1, such that Tikhonov Regularization is defined for every $\lambda > 0$ and every b in solution space U for which

$$\|b - b_{exact}\|_2 \leq \delta \leq \delta_1$$

  and

- There exists a function $\lambda = \lambda(\delta)$ of δ such that, for every $\varepsilon > 0$, there exists a number $\delta(\varepsilon) \leq \delta_1$ such that the inclusion $b_\delta \in U$ and the inequality

$$\|b_{exact} - b_\delta\| \leq \delta(\varepsilon)$$

  imply

$$\|x_{exact} - x_\lambda\| \leq \varepsilon$$

This means that if the noise from the measurement is less than δ_1, then λ is a function of δ. This also implies that in order for the regularization method and our self-constrained method to work, the noise must be in a certain range, as will be shown in the numerical analysis section. Physically this simply means that if the data is sufficiently noisy, the regularization method fails to provide a unique solution because the noise is sufficiently large to span multiple solutions in solution space.

We assume that all the error comes from the Eq. (5.2) is from the right hand side b, such as

$$b = b^{exact} + \varepsilon$$

.

In order to obtain the regularized result of the Eq. (5.4) with the noise based right hand side b, we need to choose the factor λ. The Discrepancy Principle shows that we should choose the factor λ such that the residual norm $\|Ax_\lambda - b\|$ equals the "discrepancy" in the data, as measured by $v_{dp}\|e\|_2$ [29], where v_{dp} is the "safety factor".

$$\|Ax_\lambda - b\|_2 = v_{dp}\|\varepsilon\|_2 \tag{5.6}$$

From Eq. (5.6), we know that the goodness-of-fit of the problem is dependent on the error from the right hand side b. The larger the error, the worse the fit. This is the main challenge of using regularization methods to solve inverse problems. If the error from the right hand side is too large, we can only choose a relatively large λ to discard the noise-dominated part, which also discard a large amount of information that could be used to reconstruct x.

5.5 Self constrained method with feedback

To solve the problem when the noise from the right-hand side b is large, we introduce a self-constrained method to pre-filter the noise. We will search the space $b \pm \eta$, where η is the standard deviation of the white noise, and find the combination can give us the least residual $\|Ax_\lambda - b\|_2$ to form the new b which is very close to b_{exact}. Then we can feed the new b into the regularization process, which can give us a better regularization result. Since

the search space is a continuous space and can be very large, we need to use a stochastic search algorithm. Evolutionary Algorithms (EA) are the most well-known stochastic search algorithms, and in this work we use EAs to search the noise space and find the smallest residual $\|Ax_\lambda - b\|_2$. The flowchart for the self-consistent regularization method with EAs is shown in Fig. 5.6.3. In the following sections, a parallel cellular evolutionary algorithm is introduced that is designed for the self-constrained method.

5.6 Parallel Cellular Evolutionary Algorithm

EAs are a family of heuristic search methods. It is a generic population-based optimization algorithm, which is inspired by biological evolution. Each individual in the population may be viewed as a representation of a particular solution to an algorithm problem. In the self-constrained inverse problem, each individual represents one possible self-constrained measurement. Selection, Crossover, and Mutation are three key operators for all evolutionary algorithms.

- **Selection**: Inspired by "survival of the fittest" from biological evolution, its aim is to select the parent according to their fitness. Therefore, the individual with above average fitness will expect to have more copies in the new population.

- **Crossover**: Once the parent is selected, the crossover is applied to form the new offspring, the most common type is single point crossover as shown in Fig. 5.6.1.

- **Mutation**: After crossover, there is a probability that the offspring individuals undergo mutation as shown in Fig. 5.6.1 . The mutation simulates the effect of transcription errors when a chromosome is duplicated from biological mutation. Its aim is to maintain genetic diversity from one generation of a population to the offspring.

Algorithm 1: Cellular Evolutionary Algorithms

1 k = 0;
2 P_k := a population of randomly-generated individuals in a cellular structure;
3 **while** *not termination condition* **do**
4   **for** *each vertex i in the cellular grid* **do**
5   evaluate fitness of individual i in P_k;
6   select individuals in its neighborhood;
7   produce offspring;
8   evaluate fitness of the offspring;
9   assign one of the offspring to vertex i;
10   **end**
11   k = k + 1;
12 **end**

Usually, EAs assume that any individual may interact with any other individual in the population. That is to say; the crossover operator can operate on any two of the individual in the population. However, this is not always the case: individuals can interact locally, instead of globally, which known as "isolated by distance." This situation is usually depicted by using a connected graph as shown in Fig. 5.6.2, in which the vertex is an individual, while edges correspond to interactions between pairs of individuals. The set of potential mates of an individual is called its neighborhood. In Fig. 5.6.2,
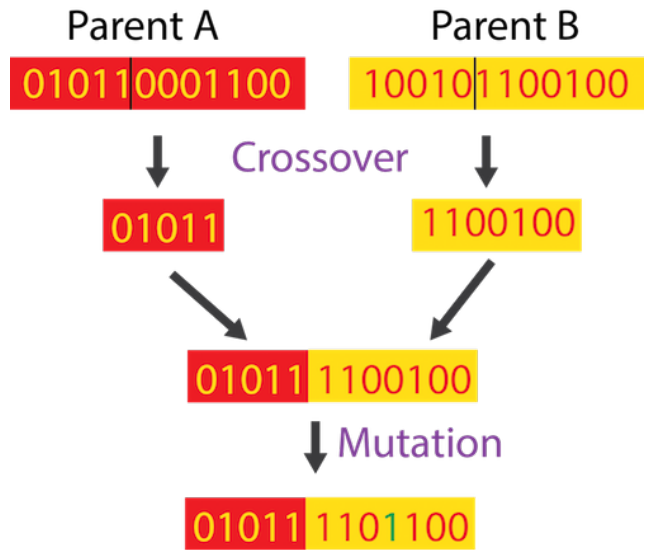
Figure 5.6.1: Apply crossover and mutation operators on the selected parent A and B.

the individual, can only interact with its nearest neighborhood. The crossover operator can operate between the individual and its neighborhood. We call these kinds of EAs that are based on these particular graph and neighborhood structure Cellular Evolutionary Algorithms (CEAs).The pseudo-code for CEAs is shown in Algorithm. 1. There are two main reasons we choose CEAs as our search and optimization method. The first reason is that we can divide the connected graph as shown in Fig. 5.6.2 into many sub-blocks, and distribute each block to the cluster for parallel computing. The second reason is that CEAs are very good at retaining the diversity of the population, preventing the search optimization from converging to the local minimum.

70
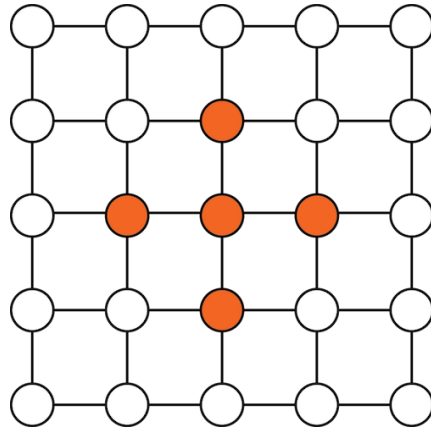
Figure 5.6.2: A grid cellular structure and neighborhood structure in CEAs.
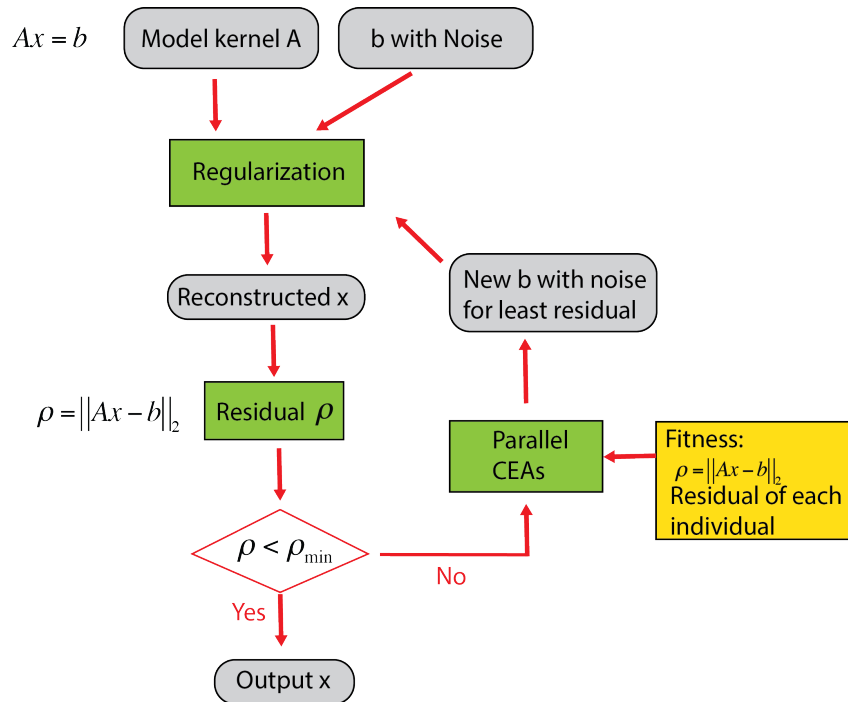
Figure 5.6.3: Self constrained regularization method (SCRM) with Evolutionary Algorithm.

5.7 PARALLEL CELLULAR EVOLUTIONARY ALGORITHMS BASED ON APACHE SPARK

5.7.1 Apache Spark

Apache Spark is a fast and general-purpose cluster computing system. It was originally developed at UC Berkeley in 2009 [83]. We choose it as our service to implement our CEAs because of it supports in-memory computing.

Fig. 5.7.1 illustrates the driver and worker model for the Spark application. Every Spark application has a driver program runs the *main* function. The *main* function is responsible to prepare the resilient distributed datasets (RDDs) and the worker function. Then the RDDs is distributed across the nodes of the cluster that can be operated on with the worker function in parallel. The RDDs is very important abstraction Spark provides. It can be created in 2 ways: the first is by directly paralyzing a collection, and the second is by reading data from an external source (S3, HDFS, etc.). The RDDs can be cached in the worker machine memory, allowing it to be reused across parallel operations. It can also automatically recover from node faller.

In the following section, we will demonstrate how we design the Parallel version of the Cellular Evolutionary Algorithms and deploy it to the cluster based on Apache Spark.

Figure 5.7.1: Apache spark driver and worker model for in-memory cluster computing

5.7.2   **Parallel Cellular Evolutionary Algorithms**

CEAs are naturally supporting by parallel computing. In this section, we will carefully design the parallel version of the CEAs to best utilize the Spark in-memory feature.

Fig. 5.7.2 shows the work flow of the Parallel CEAs ruining on the cluster based on Apache Spark. We first initialize the individual in the population grid and divide it into sub-grid which with the common boundary as shown in the figure in the *main* function. Then the sub-grid is saved to the RDDs, and we distribute the RDDs with worker function (PCEAs as shown in Algorithm. 2) to the worker machine in the cluster. In the worker machine, the RDDs which store the sub-grid is operated on with the PCEAs worker function in parallel. We will get the updated sub-grid which is then collected by the *main* function in the driver machine to form the updated population grid. Finally, we will check whether the termination condition is satisfied. If it is yes, then we give out the population grid. If it is not, then we repeat the whole process with the updated population grid.

In line 2 and line 5 of Algorithms. 2, we need to evaluate the fitness function for our particular problem. In the ill-posed inverse problem, the fitness function is the residual of the regularization reconstruction. The detail of which will be described in the following section with a one-dimensional image restoration model test problem.

74
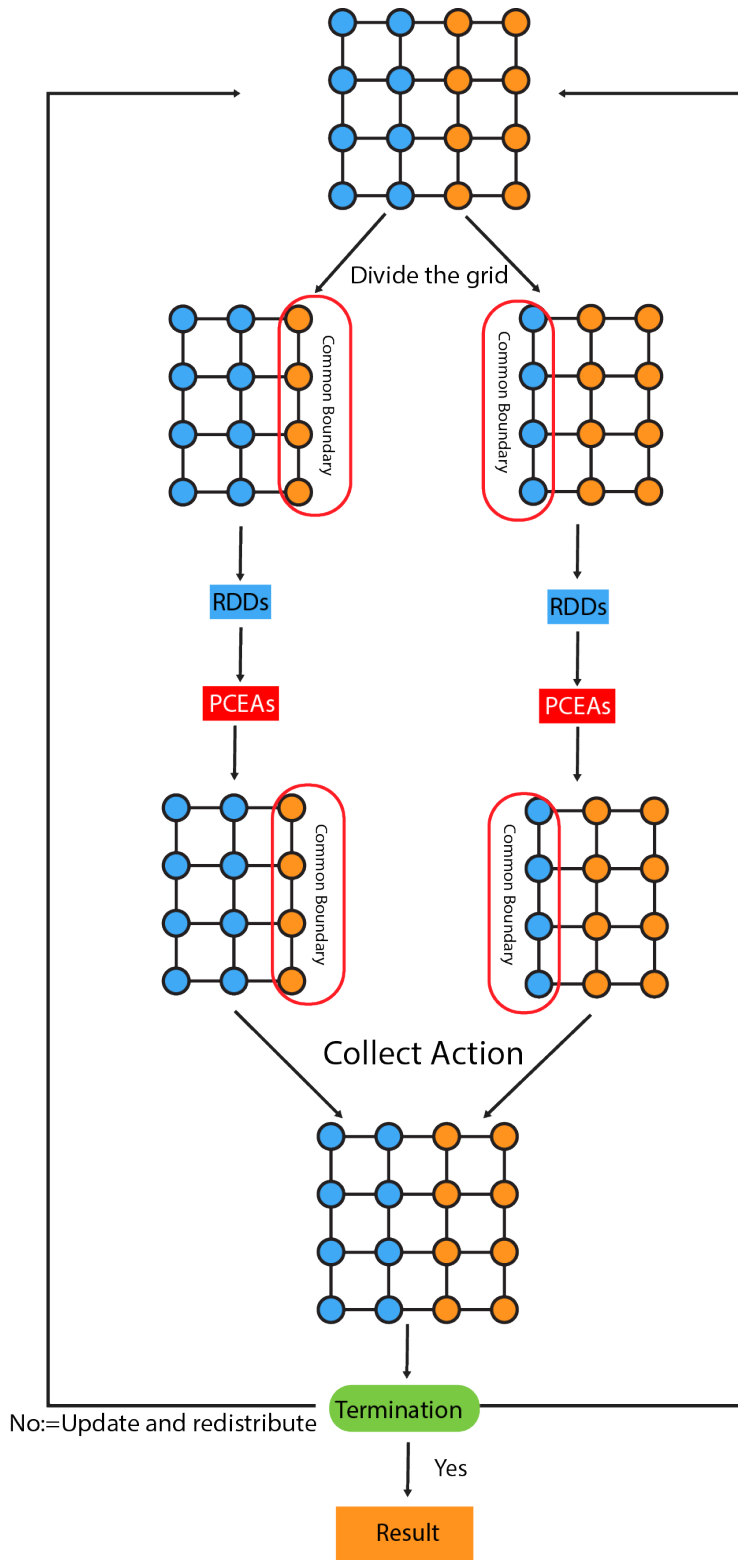
Figure 5.7.2: Parallel Cellular Evolutionary Process based on Apache Spark.

Algorithm 2: Parallel Cellular Evolutionary Algorithms for sub-grid
1 for *each vertex i in the cellular sub-grid* **do**
2   evaluate fitness of individual i in P_k;
3   select individuals in its neighborhood;
4   produce offspring;
5   evaluate fitness of the offspring;
6   assign one of the offspring to vertex i;
7 end

5.8 NUMERICAL RESULTS AND DISCUSSION

In order to demonstrate the benefits and reliability of our methods, we will it use to solve a test inverse problem: the one-dimensional image restoration model test problem that assumes $\phi(t)$ as shown in Eqs.5.8 and 5.9 the source's light intensity as a funtion of the angle s of the incidence. Letting $K(s,t)$ as shown in Eq. (5.8) to be the point spread function for an infinitely long slit with a width equal to one wavelength, the basic relation between the source light intensity $\phi(t)$ and the observed light intensity in the image produced on the other side of the slit $f(s)$ is

$$f(s) = \int_{-\pi/2}^{\pi/2} K(s,t)\phi(t)dt \qquad (5.7)$$

in which

$$K(s,t) = (\cos(s) + \cos(t))^2 \left(\frac{\sin(\pi(\sin(s) + \sin(t)))}{\pi(\sin(s) + \sin(t))} \right)^2 \qquad (5.8)$$

76

Where $-\pi/2 \leq s, t \leq \pi/2$, while the source's light intensity as a function of the angle t

$$\phi(t) = 2\exp(-6(t-0.8)^2) + \exp(-2(t+0.5)^2) \qquad (5.9)$$

These equations model the situation where light passes through an infinitely long slit.

This problem can easily be mapped onto our self-constrained regularization method with the evolutionary algorithm. The light intensity in the image produced on the other side of the slit is assigned to b in Eq. (5.2), and the known point spread function is assigned to matrix A in Eq.5.2, and we want to reconstruct the source's light intensity (x in Eq. (5.2)) as a function of the angles as t.

Fig.5.8.1 shows the Picard plots for the one-dimensional image restoration model test problem with different white noise levels. From the figure, we can see that the Discrepancy Principle is verified as shown in Eq. (5.6).

Since we already know the kernel K and we are assuming that the incoming light has the form as shown in Eq. (5.9), we can calculate the "exact" b without noise using Eq. (5.2). In the following example, we add a random white noise (with standard deviation $= 0.5$) on the first three points in b (discretization size is 40). Fig.5.8.2, (a) shows the result when we directly apply the regularization method on the measurement b without first
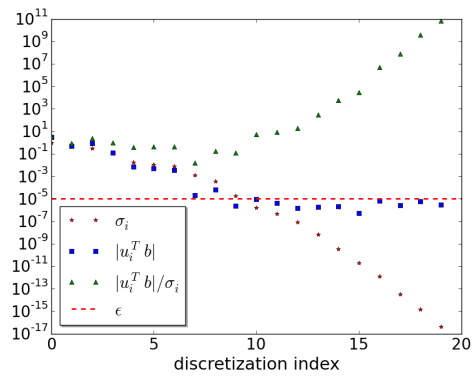
(a) noise 1e-5
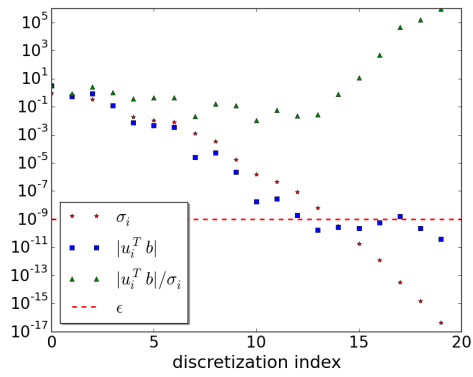
(b) noise 1e-9
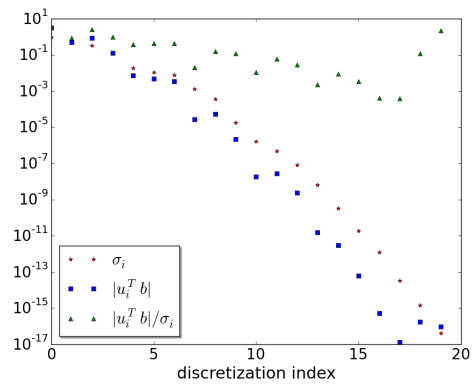
(c) no noise

Figure 5.8.1: The Picard plots for the one-dimensional image restoration model test problem with different noise levels. Random white noise level is shown by the red dashed line.(a) With an additional white noised added to the measured b (1e-5).(b) With an additional white noised added to the measured b (1e-9).(c) With no added noise (only discretization noise).

78
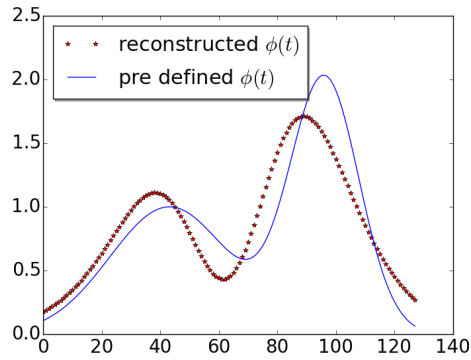
(a) Without noise reduction, residual = 0.250
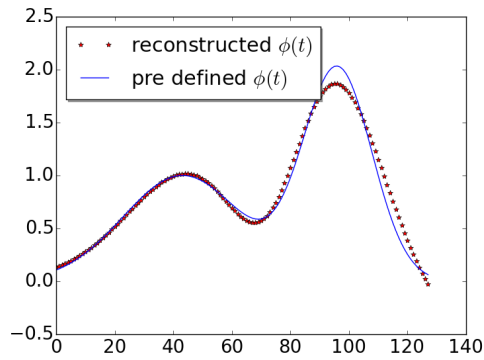
(b) noise reduction after 1 genreation, residual = 0.005
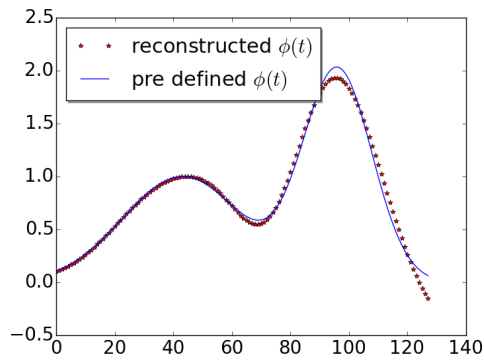
(c) noise reduction after 10 generation, residual = 5.288e-4

Figure 5.8.2: Reconstructed $\phi(t)$ for one-dimensional image restorations model. Blue curves: the exact solution, Red Point: the reconstructed result (a) Without Cellular Evolution Algorithms(CEAs) noise reduction. residual $\|Ax - b\|_2 = 0.250$ (b) With 1 generation CEAs noise reduction, residual $\|Ax - b\|_2 = 0.005$, (c) With 10 generation CEAs DeNoise, residual $\|Ax - b\|_2 = 5.288e-4$

applying the SCIIP method, (the noise on the first three points is 0.5, -0.5, 0.4), and the residual is 0.250 for this case. Fig.5.8.2 (b) shows the result when we use our self-consistent regularization method with Cellular Evolutionary Algorithms(CEAs) for 1 generation(the noise on the first three points reduce to -0.006, -0.007, -0.007), the residual is 0.005 for this case. Fig.5.8.2(c) shows the result when we use our SCIIP method with Cellular Evolutionary Algorithms(CEAs) for ten generations (the noise on the first three points reduce to -8.6e-4, -8.7e-4, 4.6e-4), the residual is 5.288e-4.

The example in the previous section showed that our SCIIP method does give a better result compared to the traditional regularization method. However, this is not always the case, since in the previous example, we assuming that the noise only exists at the first three point of the b.

The success of the SCIIP method requires the existence of a unique solution for b within the search space. Otherwise, the self-constrained regularization can yield multiple answers for b, as shown in Fig. 5.8.3. We use the same example as in the previous section. This time, the discretization size is 40 points, and we assume that the noise only exists on the first 20 points. The initial guess b is generated randomly in the b search range. In Fig. 5.8.3 (a), the search range is $b - 0.1 < b < b + 0.2$ and in Fig. 5.8.3 (b), the search range is $b - 2 < b < b + 1$. As seen, in Fig. 5.8.3 (a), when the search range is relatively small, we obtain a result from the SCIIP that is very close to the exact answer after only five generations. In Fig. 5.8.3 (b), as we increase the b search range, we obtain another self-constrained b solution other than the exact b, which means that the self-constrained b is not unique

in the search range. Fortunately, we can simply discard this solution, since, in this case, the result is nonphysical because it has negative b value.

Fortunately, in practice, there are many conditions that enable us to narrow the b search space and obtain unique solutions:

- The standard deviation of the noise on b is usually very small compared to b.

- The large noise usually only exists on some part of the measurement, such as the low-frequency or high-frequency part.

5.9 Summary and Outlook

In summary, we have demonstrated a new method for improving the signal-to-noise method compared to the result obtained by applying the standard regularization method to ill-posed problems. We have applied this method to a one-dimensional image restoration model test problem. In the test problem, we reduce the residual from 0.250 to 0.005 with only 1 generation of CEAs. This work has the potential to improve the accuracy of inverse problem reconstruction solutions in a wide range of fields.
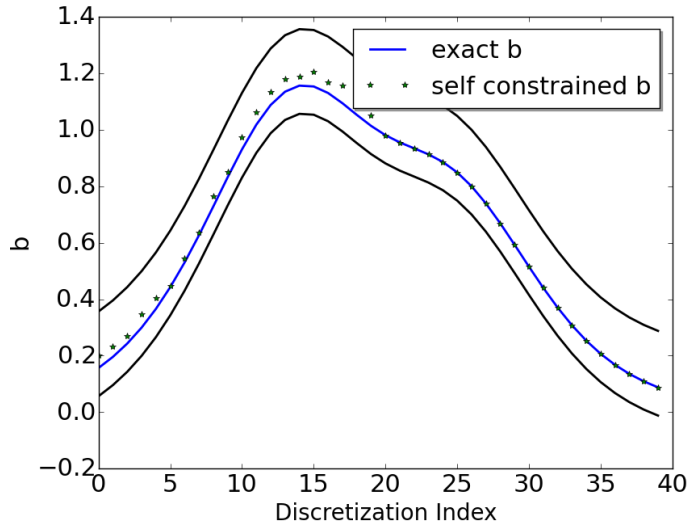
(a) b search range: $b - 0.1 < b < b + 0.2$
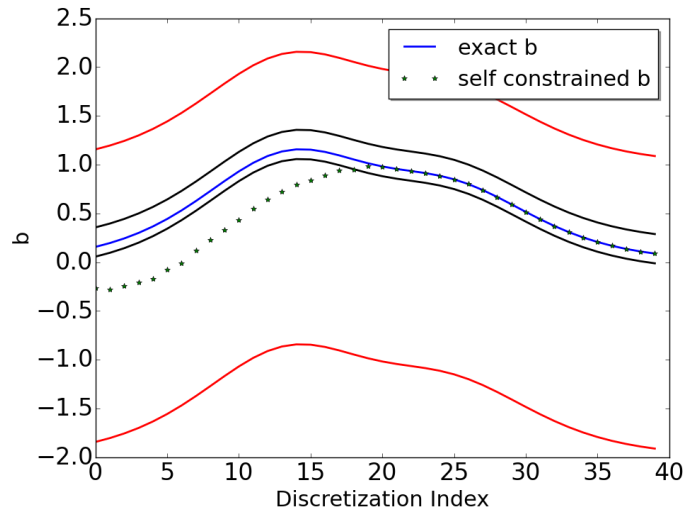
(b) b search range: $b - 2 < b < b + 1$

Figure 5.8.3: Self constrained b in the b search range. The initial guess b is generate randomly in the b search range. The blue line is the exact b, and the green * is the self constrained b. The discretization size is 40 points, we assuming that the noise only exist on the first 20 point. In both cases, we ran 5 generations of the genetic algorithm.(a) b search range: $b - 0.1 < b < b + 0.2$, the range is between the two black lines. (b)b search range: $b - 2 < b < b + 1$, the range is between the two red lines.

CHAPTER 6

INDEX-MATCHED IWKB METHOD FOR THE
MEASUREMENT OF SPATIALLY VARYING RE-
FRACTIVE INDEX PROFILES WITHIN THIN-
FILM PHOTOVOLTAICS

6.1 INTRODUCTION

The performance of many thin-film photovoltaics (PV) is significantly influenced by the variation of material properties throughout the depth (i.e., the vertical, or, substrate-normal, direction) of the photoactive layer. Examples of the spatial variation of the photoactive layer material properties include grading of the Ga concentration (and concomitantly the bandgap energy) in copper indium gallium selenide $(Cu(In_{1-x},Ga_x)Se_2 - \text{CIGS})$ solar cells [47], as well as vertical phase segregation gradients (donor/acceptor ratios that vary with depth) in bulk heterojunction organic photovoltaics

(OPVs)[3, 21]. The accurate measurement of the resulting "depth profiles" for optical and electronic properties such as refractive index [26] and charge collection probability [15, 37, 61, 62] is critical to the understanding, modeling, and optimization of these devices. Moreover, in many cases, the optical refractive index profile alone can yield information on depth-dependent material variation from which the depth profile of electronic properties can be inferred [39, 48].

In this chapter, we describe a novel method, which we refer to as index-matched IWKB (IM-IWKB), for the reconstruction of refractive index profiles (RIPs) with high spatial resolution within the photoactive layers of thin-film photovoltaics for films as thin as 200 nm. While the Inverse Wentzel-Kramers-Brillouin (IWKB) method has been used in the past to successfully reconstruct RIPs of various films [8, 11, 64, 85], this approach is only valid for relatively thick (larger than 2 μm) films for visible wavelengths, since the number of points in the reconstructed RIP is equal to the number of modes supported by the film at that wavelength. For the ultra-thin layers relevant to many thin-film photovoltaics (typically 100 nm – 200 nm for OPVs, for example), it is either impossible to reconstruct the profile at all, or the result of the reconstruction has poor spatial resolution due to the low number of guided modes.

The IM-IWKB method described below deposits a relatively thick (1-10 μm) index-matched, non-absorbing layer below the thin photoactive layer of interest, and then applies the IWKB method to this system, resulting in a spatial resolution for the reconstruction of the RIP that is

84

improved by more than a factor of ten compared to the traditional IWKB without the use of an index-matched layer. While RIPs for such thin layers can be obtained using spectroscopic ellipsometry with multiple-layer models [3, 21], our approach requires no free parameters, which is a significant advantage compared to the parameterized, model-based technique used in ellipsometry. This allows for much higher spatial resolution using our approach compared to ellipsometry, where the number of free parameters necessarily increases with the desired spatial resolution.

Below we first describe the mathematical basis of our approach, and then apply it to a computational example that assumes a RIP of a "canonical" OPV system to demonstrate the method's accuracy and limitations for the typical system of interest. Finally, we describe our experimental implementation of this method and results for OPV devices fabricated in our lab.

6.2 Methodology

6.2.1 Index-matched IWKB (IM-IWKB) for improved spatial resolution

Consider a monotonically decreasing refractive index profile consisting of the glass substrate, index-matched layer, photoactive layer, and air as shown in Fig. 6.2.1.According to the IWKB method [11], the characteristic

equation of the ith mode is given by

$$k \int_0^{x_i} [v^2(x) - N_i^2]^{\frac{1}{2}} dx = (i-1)\pi + \phi_0 + \phi_t, i = 1, 2, 3...$$ (6.1)

$$n(x_i) = N_i$$ (6.2)

$$v(x) = \left\{ \begin{array}{cc} n(x) & (TE) \\ n(x)[1 + \frac{n(x)n(x) - 2n^2(x)}{k^2 n^4(x)}] & (TM) \end{array} \right\}$$ (6.3)

where n(x) is the actual refractive index profile as a function of position x, $N_i = \beta_i/k$ is the effective index of the ith order mode with propagation constant β_i, $k = 2\pi/\lambda$ is the free space wavenumber, is the free-space wavelength of light, x_i is the turning point position of the $i_t h$ order mode as given by Eq. 6.2, x_0 and N_0 are the turning point and effective index of the glass substrate, and ϕ_0 and $\phi_i \equiv \phi_t = cons \tan t$ (for all i) are the phase contributions from the turning points x_0 and x_i [11]. The profile is assumed to be monotonically decreasing (true for the experimental case of an OPV bulk heterojunction that we consider later), and therefore the first turning point (x_0) is always located at the beginning of the structure (the interface between substrate and index-matched layer in this case). The values of ϕ_0 and ϕ_t are given by

$$n(x_i) = N_i$$ (6.4)

86
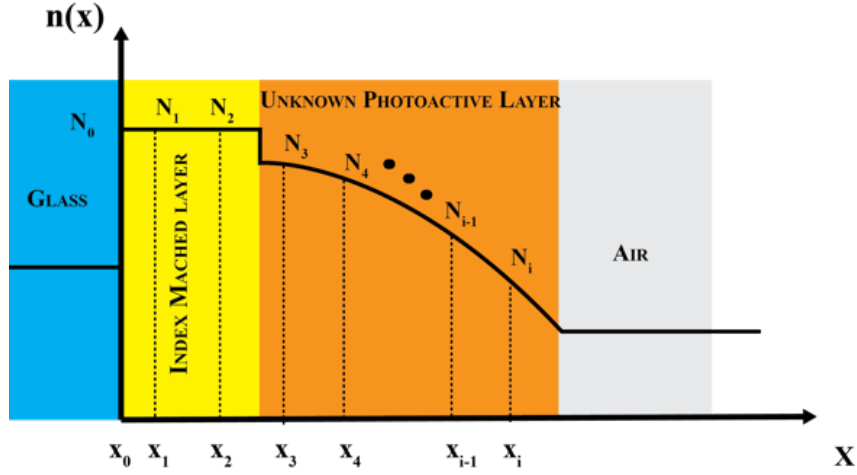
Figure 6.2.1: Refractive index profile n(x) of an index-matched layer and an unknown photoactive layer on a glass substrate, as a function of position x. (N_i, x_i) represents the (effective index, turning point) for guided mode i.

$$\phi_0 = \tan^{-1}\left\{ r_0 \left[\frac{N_i^2 - n_{glass}^2}{N_0^2 - N_i^2} \right]^{\frac{1}{2}} \right\} \tag{6.5}$$

where $r_0 = 1$ for transverse-electric (TE) modes, and $r_0 = (N_0/n_{glass})^2$ for transverse-magnetic (TM) modes.

The recursive equation

$$x_i = \frac{(i-1)\pi + \phi_0(N_i) + \phi_t - \sum_{j=1}^{i-1} k \left\{ x_j \left[(N_{avg,j}^2 - N_i^2)^{1/2} - (N_{avg,j+1}^2 - N_i^2)^{1/2} \right] \right\}}{k(N_{avg,i}^2 - N_i^2)^{1/2}}, i = 1,2,3 \tag{6.6}$$

where $N_{avg,i} = (N_i + N_{i-1})/2$, relies on backward averaging of the effective indices to obtain values between the measured ones. To verify the reliability of our IM-IWKB method in the Numerical Results section below, we use Finite-Difference Time-Domain (FDTD) calculations [67] to construct a

sample structure with a known RIP and solve for the effective indices of the guided modes. These effective index values are then used to reconstruct the RIP using the IM-IWKB method outlined above. In the Experimental Results section below, the effective index values of a test structure are measured using prism coupling [16, 71, 76], and these values are then used to reconstruct the RIP using the IM-IWKB method outlined above. It is important to note that if the index gradient of the photoactive layer was in the opposite direction (highest index at the air-layer interface and lowest at the substrate-layer interface), then we would need to put the index-matched layer between the photoactive layer and the air.

Experimentally, we use a prism coupler (Metricon Model 2010) to measure the effective indices of the guided modes in a sample, as shown in Fig. 2.5.6[16, 76].

6.2.2 SAMPLE PREPARATION AND CHARACTERIZATION

The test films used for the experiments shown in Fig. 6.4.1 were deposited on the AlN side of AlN (5 m $\pm$ 5%thicknesses were used)/sapphire(430 μm) substrates (Kyma Technologies, wafer ID:B6523-1). The thickness of the AlN layer was determined by spectroscopic ellipsometry. The RMS surface roughness of the AlN is 50 nm. The test photoactive layer films were bulk heterojunction (BHJ) layers that are typically used as the photoactive layer in OPVs, consisting of solution-processed 1:1 ratio poly(3-hexythiophene-2,5-diyl) (P3HT) and phenyl-C61-butyric acid methyl ester (PCBM) (20 mg/ml) in dichlorobenzene solvent [15]. The

88

P3HT:PCBM was spin-coated (700 rpm for 40 s) on the AlN. The devices were thermally annealed at 150 °C for 10 min in a glove box for post-processing before measurement. Although we use a sapphire substrate in these experiments, any substrate can be used as long as it has minimal absorption at the wavelength of interest, and as long as its refractive index is lower than the lowest refractive index of the photoactive layer. We choose AlN as the index-matched layer for the following reasons: (1) The refractive index (n = 2.0039) of AlN is higher than and very close to the highest refractive index of the P3HT:PCBM photoactive layer. To use the IM-IWKB method, the refractive index of the whole structure (including the index-matched layer) should decrease monotonically. Therefore the refractive index of the index-matched layer should be higher than the highest refractive index of the P3HT:PCBM photoactive layer. (2) The thickness of the index-matched layer (AlN, 5 μm) should be large enough to obtain a sufficiently large number of data points.

6.3 NUMERICAL RESULTS AND DISCUSSION

To demonstrate the benefits and reliability of our methods, we use FDTD calculations [67] to simulate a sample structure with a known RIP and solve for the effective indices of the guided modes. We first consider the structure: substrate(semi-infinite thickness, refractive index n = 1.76)/index-matched layer(1 μm, 5 μm, 20 μm, n = 1.93)/photoactive layer(1 μm)/air shown in Fig. 6.3.1(a) at a wavelength of 500 nm. For this example, all layers are considered to be non-absorbing (purely real refractive

index), including the RIP of the 1 μm photoactive layer, which is defined as $n_{PA}(\text{x}) = 1.93 - 0.13(x/t_{PA})^2$ (shown as the black line labeled "Actual Profile" in Fig. 6.3.1(a)), where t_{PA} is the thickness of the photoactive layer, and x is the position within the photoactive layer with x = 0 representing the photoactive-layer-index-matched-layer interface. From Fig. 6.3.1(a), we see that by varying the thickness t_{IM} of the index-matched layer, we can increase the spatial resolution and accuracy of the reconstruction $-$ (0.0095, 0.0072, 0.0068) are the root mean squared differences, Δ_{RMS}, between the reconstructed profile and the actual profile, and (200nm, 63nm, 33nm) are the spatial resolutions (spacing between successive points in the reconstruction) for (1 μm, 5 μm,10 μm) thick index-matched layers, respectively. In this reconstruction, the deviations of the higher-order modes near the air interface from the actual profile become larger because the phase contributions from the turning points near air interface are not exactly $\pi/4$ due to the weaker confinement of these modes.

Next we consider the structure: substrate(semi-infinite, n = 1.76)/index-matched layer(t_{IM} = 10 µm, n = 1.93)/photoactive layer(t_{PA} = 1 µm, parabola (Δ_{RMS} = 0.0068), exponential (Δ_{RMS} = 0.0147), Gaussian((Δ_{RMS} = 0.0090) profile)/air in Fig. 6.3.1(b) in order to test the performance of the IM-IWKB method works for different profiles. As shown in Fig. 6.3.1(b), the IM-IWKB method performs well for any functional form, as long as that form satisfies the slowly varying constraint of the WKB method.

Next we consider the structure: substrate(semi-infinite, n =
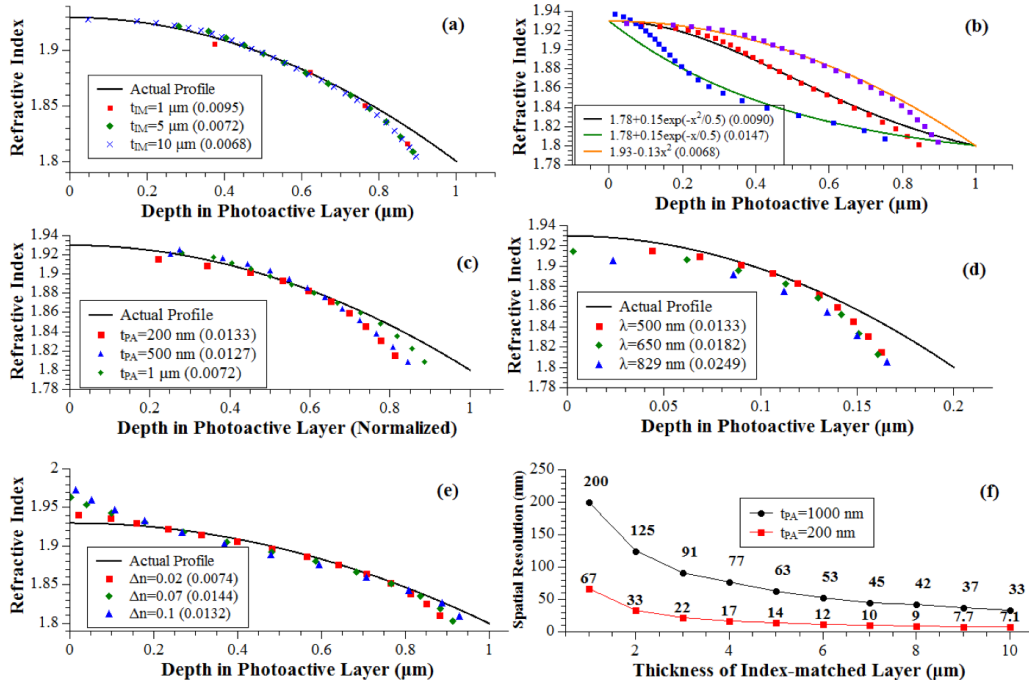
Figure 6.3.1: Reconstructed RIPs for TE-polarized light performed by the IM-IWKB method using guided mode effective indices obtained via FDTD simulation for the structure: substrate(semi-infinite, n = 1.76)/index-matched layer(thickness t_{IM}, n = 1.93)/photoactive layer(thickness t_{PA}, "Actual Profile" (solid black line): $n_{PA}(x) = 1.93 - 0.13(x/t_{PA})^2$ unless otherwise stated)/air. Wavelength λ assumed to be 500 nm unless otherwise stated. The number in parentheses in the legend is the root mean squared difference between the reconstruction and the actual profile. (a) $t_{IM} = (1\ \mu m,\ 5\ \mu m,\ 10\ \mu m)$; $t_{PA} = 1\mu m$. (b) $t_{IM} = 10$ m; $t_{PA} = 1\mu m$, $n_{PA}(x) = $ (parabolic, exponential, Gaussian). (c) $t_{IM} = 5$ m; $t_{PA} = (200\ nm,\ 500\ nm,\ 1\ \mu m)$ normalized to 1. (d) $t_{IM} = 5\ \mu m$; $t_{PA} = 200\ nm$; $\lambda = (500\ nm,\ 650\ nm,\ 829\ nm)$. (e) $t_{IM} = 5\mu m$, $n_{IM} = (1.95,\ 2.0,\ 2.03)$, $\Delta n = (0.02,\ 0.07,\ 0.1)$; $t_{PA} = 1\ \mu m$. (f) Spatial resolution (defined as the average spacing between successive points in the reconstruction) for the IM-IWKB reconstruction $t_{IM} = 1\text{-}10\ \mu m$; $t_{PA} = (1\ \mu m,\ 200\ nm)$.

1.76)/index-matched layer($t_{IM} = 5$ m, n = 1.93)/photoactive layer($t_{PA} = 200$ nm, 500 nm, 1 μm)/air in Fig. 6.3.1(c) at a wavelength of 500 nm. From the figure, we see that Δ_{RMS} gets larger as the photoactive layer becomes thinner. However, the reconstruction is still very accurate for a 200 nm photoactive layer ($\Delta_{RMS} = 0.0133$). Decreasing the laser wavelength can also increase the spatial resolution and accuracy of the reconstruction. Figure 6.3.1(d) demonstrates this effect for the structure: substrate(semi-infinite, n = 1.76)/index-matched layer(5 μm, n = 1.93)/photoactive layer(200 nm)/air at laser wavelengths of 829 nm ($\Delta_{RMS} = 0.0249$), 650 nm ($\Delta_{RMS} = 0.0182$) and 500 nm ($\Delta_{RMS} = 0.0133$). The absorption spectrum of the material used in the structure is the key limitation to determining which wavelengths are experimentally feasible. Wavelengths that are strongly absorbed cannot be used to measure the effective indices since the minimum in the reflected signal that indicates the effective index becomes increasingly difficult to identify with increasing absorption.

In the experiment setup, the refractive index of the photoactive layer at the index-matched-layer interface (n_{PA}(x = 0)) and the refractive index of the index-matched layer (n_{IM}) are not matched perfectly. If the IM-IWKB method is used on such a profile, there will be an error introduced because the slowly varying assumption of the IWKB method is violated at this interface. However, if we can make the refractive index step (Δn = $n_{IM} - n_{PA}$(x = 0)) at the interface small enough, the introduced error can be neglected as shown in Fig. 6.3.1(e). The structure assumed in Fig. 6.3.1(e) is: substrate(semi-infinite, n = 1.76)/index-matched layer(5 μm with Δn =

0.02, 0.07 and 0.1 refractive index steps)/photoactive layer(1 μm)/air. From Fig. 3(e), we see that while step sizes of $\Delta n = 0.1$ and $\Delta n = 0.07$ yield relatively large Δ_{RMS} values (0.0132 and 0.0144, respectively), reducing the step to $\Delta n = 0.02$ improves the accuracy of the reconstruction ($\Delta_{RMS} = 0.0074$).

Finally, in Fig. 6.3.1(f) we show that the spatial resolution of the IM-IWKB method increases with increasing thickness of the index-matched layer. The spatial resolution is defined as the average spacing between successive points in the reconstruction, and is calculated by dividing the thickness of the photoactive layer by the number of modes whose turning points lie within the photoactive layer. Relative to the case of a $1\mu m$ thick index-matched layer, a $10\mu m$ thick index-matched layer improves the spatial resolution of the reconstruction for the 1 μm and 200 nm thick photoactive layers by a factor of 6 and 9.4, respectively.

6.4 EXPERIMENTAL RESULTS AND DISCUSSION

The bulk-heterojunction active layers that are typically employed in OPV devices are comprised of a mixture of electron donor and electron acceptor materials [81]. A canonical material choice for a OPV photoactive layer employs poly(3-hexythiophene-2,5-diyl) (P3HT) as the electron donor and phenyl-C61-butyric acid methyl ester (PCBM) as the electron acceptor. In this section, we describe experiments that use the IM-IWKB method to reconstruct the RIP of P3HT:PCBM bulk heterojunction photoactive layers. These experiments use a prism coupler to measure the guided-mode effective

indices (as shown in Fig. 2.5.6) of P3HT:PCBM thin-film samples on top of an indexed-matched layer of AlN, and then use these effective indices as input to the IM-IWKB reconstruction technique. It is well known that these layers exhibit vertical phase segregation gradients (donor/acceptor ratios that vary with depth) [3, 21]. From knowledge of the refractive indices of pure P3HT (1.780 for TE polarization at a wavelength of 829 nm) and pure PCBM (1.95425 for TE at 829 nm) obtained via spectroscopic ellipsometry, the RIP measured using IM-IWKB, and Bruggeman effective medium theory [33], we obtain the concentration depth profiles for PCBM and P3HT throughout the photoactive layer. In order to take into account the influence of annealing on P3HT due to the change in crystallinity, the pure P3HT is also thermally annealed at 150°C for post processing prior to measurement. Fig.6.4.1(a) presents measurements of the reflected light intensity at 829 nm for TE polarization as measured by the prism coupler setup shown in Fig. 2.5.6. For the structure: sapphire(430 μm)/index-matched layer(AlN, $t_{IM} = 5\ \mu m \pm 5\%$)/photoactive layer (P3HT:PCBM, 200 nm)/air, the reflected intensity shows 13 minima, each of which corresponds to a guided mode effective index. From these 13 effective index values, we use the IM-IWKB method described above to reconstruct the RIP as shown in Fig. 6.4.1(b). The thickness of the index-matched layer is around 5.3 μm from ellipsometry measurements and by subtracting this thickness from the thickness of the entire structure, we can obtain the RIP in the photoactive layer region as shown in Fig. 6.4.1(c). From the reconstructed RIP, we measure that the refractive index of the P3HT:PCBM photoactive layer changes from 1.98 to

94

1.8, in going from the index-matched layer interface to the air, and that the thickness is around t_{PA} » 170 nm (5.3 μm to 5.47 μm), While ellipsometry measurements yield $t_{PA} = 200$ nm, from Fig. 6.3.1(d), we see that the thickness of the photoactive layer (200 nm) suggested by the reconstructed RIP underestimates the actual thickness by about 30nm. The refractive index of index-matched layer (AlN) is 2.0039±0.0001 as measured by single-film prism coupler measurements. There is a refractive index step Δn $(2.0039 - 1.977) = 0.0269$ between the index-matched layer and photoactive layer, since we know from Fig. 6.3.1(e), that the highest refractive index (1.977) at the index-matched layer-photoactive-layer interface is overestimated. As mentioned earlier, the P3HT:PCBM films are typically thermally annealed at 150 °C for 10 min in a glove box for post processing prior to measurement. Fig. 6.4.1(d) shows the reconstructed RIP of the structure: sapphire(semi-infinite)/index-matched layer(AlN, $t_{IM} = 5.3$ μm)/photoactive layer (P3HT:PCBM, 200 nm)/air with and without thermal annealing, demonstrating that the slope of the RIP with annealing is larger than that without annealing. From these RIPs, and knowledge of the refractive indices of pure PCBM (1.954 for TM and TE at 829 nm) and P3HT (1.596 for TM and 1.780 for TE at 829 nm), we use Bruggeman effective medium theory as shown in Eq. 6.8 and 6.8 (where v_{P3HT} and v_{PCBM} are the volume fractions of P3HT and PCBM, and n_{P3HT} and n_{PCBM} are the refractive indices of pure P3HT and pure PCBM) [33] to determine the depth profile of the PCBM volume fraction in the photoactive layer, as

shown on the right-hand vertical axis in Fig. 6.4.1(d).

$$v_{P3HT}\frac{n_{P3HT} - N_i}{n_{P3HT} + 2N_i} + v_{PCBM}\frac{n_{PCBM} - N_i}{n_{PCBM} + 2N_i} = 0, i = 1, 2, 3... \tag{6.7}$$

$$v_{P3HT} + v_{PCBM} = 1 \tag{6.8}$$

6.5 Summary and Outlook

We have demonstrated a new method (IM-IWKB) for reconstructing the depth-dependent refractive-index profile in thin films (200 nm) with high spatial resolution (10 nm possible at a wavelength of 500 nm) by depositing a relatively thick index-matched layer (1-10 μm) adjacent to the thin film of interest and applying the Inverse Wentzel-Kramers-Brillouin (IWKB) method. We have applied this method to 200 nm thick bulk heterojunction layers of P3HT:PCBM, a common absorber layer used in OPVs and shown that by combining the RIP reconstruction with effective medium theory, the depth dependent profiles of the donor (P3HT) and acceptor (PCBM) volume fractions can also be determined. By reconstructing the volume fraction profile both before and after the annealing of the P3HT:PCBM layer, we were able to measure directly, with high spatial resolution, the evolution of phase segregation of the P3HT and PCBM phases during the annealing process. In comparison with alternative approaches such as ellipsometry, the
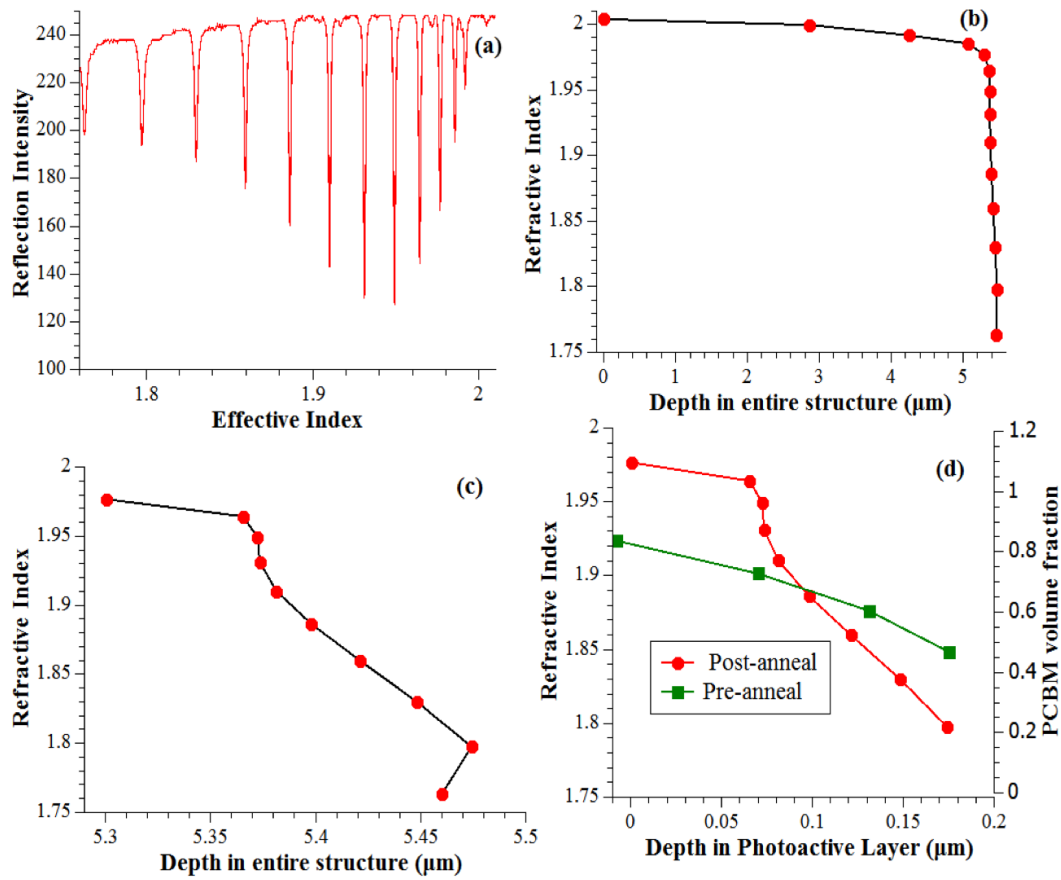
Figure 6.4.1: Experimental reconstruction of the RIP by the IM-IWKB method, using guided mode effective indices measured the prism coupler setup shown in Fig. 2.5.6. (a) Reflection spectrum for structure: sapphire(430 μm)/index-matched layer(AlN, $t_{IM} = 5.3\ \mu m$)/photoactive layer (P3HT:PCBM, 200 nm)/air. (b) RIP reconstruction for the structure in (a). (c) RIP reconstruction of the photoactive layer region for the structure in (a). (d) RIP reconstruction for the structure in (a) with (red) and without (green) thermal annealing. In panels (d), the right-hand axis shows the PCBM volume fraction calculated from the RIP by applying Bruggeman effective medium theory as described in the text.

IM-IWKB method achieves high spatial resolution with no free parameters as it reconstructs the refractive index profile by applying the IWKB method to direct measurements. The IM-IWKB technique applies to any thin film, including the photoactive layers of a many thin-film photovoltaics, and we believe it has the potential to be a broadly useful and non-destructive technique for measuring optical and material properties with high spatial resolution.

Chapter 7

Modified Index-matched IWKB with a Correction to the Phase Contribution

7.1 Introduction

In Chapter. 6, We introduced the Index Matched Inverse Wentzel-Kramers-Brillouin (IM-IWKB) Method as a new technique for the reconstruction of refractive index profiles (RIPs) with high spatial resolution within the photoactive layers of thin-film photovoltaics for films as thin as 200 nm [54].

The previous demonstration of both the IWKB and the IM-WKB methods assume a constant phase shift equal to $\pi/4$ at the turning point in the film. For thick films where IWKB is applicable, this approximation is justified. However, the assumption of a phase shift of $\pi/4$ becomes
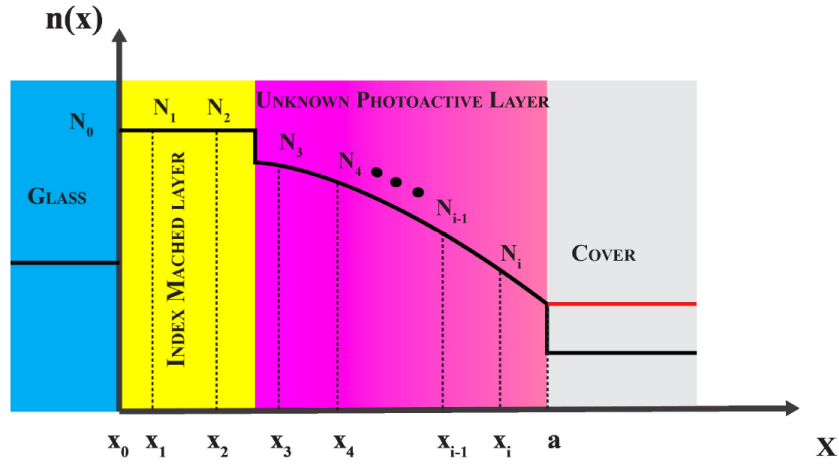
Figure 7.1.1: Refractive index profile n(x) considered in our calculations. Red (Black) line: Index profile that is continuous (discontinuous) at x=a. (N_i, x_i) represents the (effective index, turning point) for guided mode i, and a represents the thickness of the index-matched layer + unknown photoactive layer.

increasingly unjustified as the thickness of the film is decreased. In the case of thin films less than one micron in thickness, for which IM-IWKB is appropriate, this assumption results in error in the reconstructed RIP.

In this Chapter, we derive a correction to this phase shift term for the case of thin films and demonstrate the improved accuracy of IM-IWKB when using this modified phase contribution compared to the standard case of $\pi/4$. We first describe the mathematical basis of our approach, and then apply it to a computational example that assumes a RIP of a "canonical" organic photovoltaic (OPV) system to demonstrate that the method with modified phase shift achieves improved accuracy.

Figure 7.1.2: Reconstructed RIPs of the photoactive layer for TE-polarized light at a wavelength of 500 nm performed by the IM-IWKB method both with and without phase modification using guided mode effective indices obtained via FDTD simulation for the structure (see Fig. 7.1.1 black line, discontinuous at x=a): substrate(semi-infinite, n=1.76)/index-matched layer (n=1.93)/photoactive layer("actual Profile" (solid black line): $n(x) = 1.93 - 0.13(x/t_{PA})^2$ unless otherwise stated)/cover= (n=1). (t_{pA}, t_{IM}) = thickness of the (photoactive layer, index-matched layer). Number in parentheses in legend is the root mean squared difference between the reconstruction and the actual profile. (a) Substrate(semi-infinite, n=1.76)/index-matched layer $(t_{IM} = 5\mu m$, n=1.93)/photoactive layer$(t_{pA} = 1\mu m)$/cover both with (red) and without (green) phase modification. (b) Substrate(semi-infinite, n=1.76)/index-matched layer $(t_{IM} = 10\mu m$, n=1.93)/photoactive layer$(t_{pA} = 1\mu m$, Gaussian profile)/cover both with (red) and without (green) phase modification. (c) With phase modification for two values of tpA (500 nm and 1 μm) for substrate(semi-infinite, n=1.76))/index-matched layer (tIM=5 m, n=1.93)/photoactive layer $(t_{pA} = 500nm$, 1 μm)/cover, with depth in photoactive layer normalized to 1. (d) Dependence of phase contribution ϕ_i on the effective index in the cases with (red square) and without (black circle) phase modification for the structure substrate(semi-infinite, n=1.76)/index-matched Layer (5 m, n=1.93)/photoactive Layer $(t_{pA} = 500nm)$/cover.
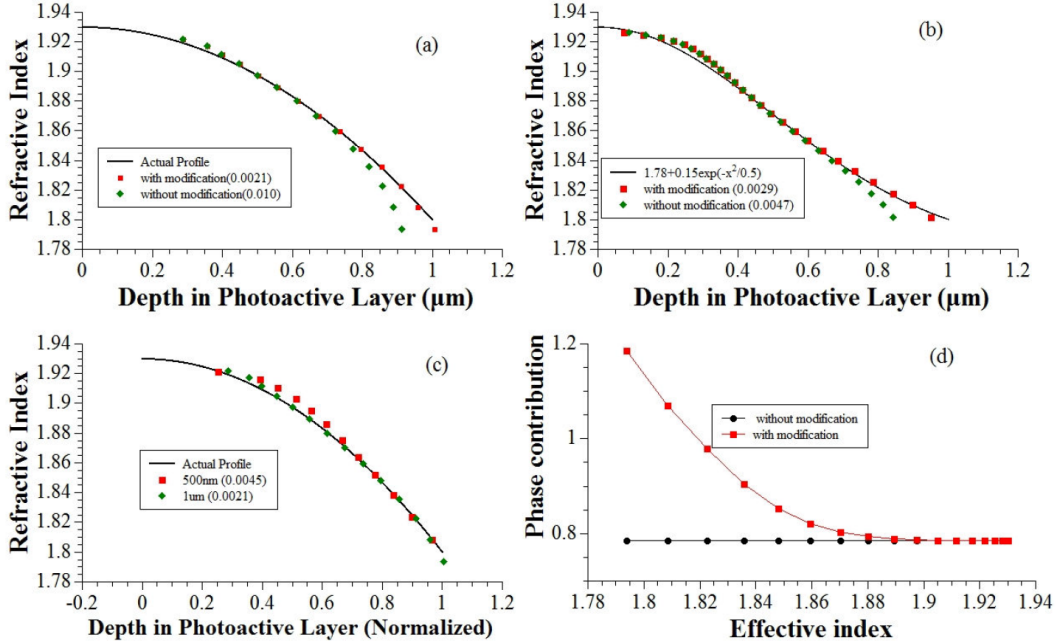
101
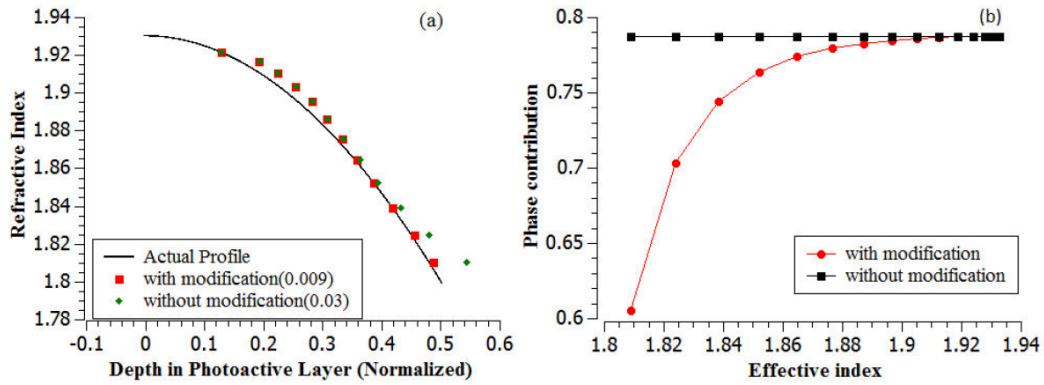
Figure 7.2.1: Reconstructed RIPs of the photoactive layer for TE-polarized light at a wavelength of 500 nm performed by the IM-IWKB method both with and without phase modification using guided mode effective indices obtained via FDTD simulation for the structure (see Fig. 7.1.1 red line, continuous at x=a): substrate(semi-infinite, n=1.76)/index-matched layer (n=1.93)/photoactive layer("actual Profile" (solid black line): $n(x) = 1.93 - 0.13(x/t_{PA})^2$ unless otherwise stated)/cover. $(t_{PA}, t_{IM}) =$ thickness of the (photoactive layer, index-matched layer). Number in parentheses in legend is the root mean squared difference between the reconstruction and the actual profile. (a) Substrate(semi-infinite, n=1.76)/index-matched layer ($t_{IM} = 5\mu m$, n=1.93)/photoactive layer ($t_{PA} = 0.5\mu m$/cover (n=1.8) both with (red square) and without (green diamond) phase modification. (b) Dependence of phase contribution ϕ_i on the effective index in the cases with (red circle) and without (black square) phase modification for the structure substrate(semi-infinite, n=1.76)/index-matched Layer (5 m, n=1.93)/photoactive Layer ($t_{PA} = 500nm$)/cover (n=1.8).

7.2 Modified Phase Contribution

The quantity ϕ_i in Eq. 6.6 from Chapter 6 represents the phase contribution from the turning point x_i. The phase contribution ϕ_i is typically assumed to be a constant value of $\pi/4$ [8], which is a good approximation for the thick-film case. However, for the case of thin films ($<$ $1\mu m$ thick) relevant to the IM-IWKB method and many thin-film photovoltaics, ϕ_i must be modified, especially for modes that have turning points near the cover interface [77].

In this chapter, to demonstrate the improved accuracy of IM-IWKB when using this modified phase shift term, the thin-film structure is divided to two cases. The first example is the structure shown in Fig. 7.1.1 (black line), where the index profile is discontinuous at x=a. For this case, the phase contribution ϕ_i is given by Eq .7.1. The second example is the structure shown in Fig. 7.1.2 (red line), where the index profile continuous at x=a, in which case the phase contribution ϕ_i is given by Eq. 7.2:

$$\phi_i = \tan^{-1}\left\{\frac{r_0 P_{a^+}[\text{Bi}(\xi_1) + \text{Ai}(\xi_1)] + \text{D}_1^{1/3}[\text{B}'_i(\xi_1) + \text{A}'_i(\xi_1)]}{r_0 P_{a^+}[\text{Bi}(\xi_1) - \text{Ai}(\xi_1)] + \text{D}_1^{1/3}[\text{B}'_i(\xi_1) - \text{A}'_i(\xi_1)]}\right\} \tag{7.1}$$

$$\phi_i = \frac{\pi}{4} + \tan^{-1}\left[\frac{P_{a^+}A_i(\xi_2) - D_2^{1/3}A_i^{'(\xi_2)}}{P_{a^+}B_i(\xi_2) - D_2^{1/3}B_i^{'(\xi_2)}}\right] \tag{7.2}$$

where $r_0 = 1$ for TE modes, $r_0 = n^2(a^-)/n^2(a^+)$ for TM modes, Ai(x)

and Bi(x) are Airy functions, and for convenience we define:

$$P^2 = k^2(N_i^2 - n^2(x))$$

$$P_{a^+} = P(x = a^+)$$

$$P_{a^-} = P(x = a^-)$$

$$D_1 = k^2[N_i^2 - n^2(x = a^-)]/(a - x_i) \quad (7.3)$$

$$D_2 = k^2[n^2(x = a^-) - N_i^2]/(a - x_i)$$

$$\xi_1 = \xi(x = a^-) = P_{a^-}^2 D_1^{-2/3}$$

$$\xi_2 = \xi(x = a^+) = P_{a^+}^2 D_2^{-2/3}$$

Now that we have derived a modified expression for the phase contribution ϕ_i, we can apply this modified IM-IWKB technique to the reconstruction of RIPs typical for P3HT:PCBM bulk heterojunction absorber layers in organic photovoltaics [54]. The RIP is reconstructed via modified IM-IWKB by the following iterative method:

1. Use IM-IWKB method ($\phi_i = \pi/4$) to determine the initial set of x_i.

2. Use the initial set of x_i and corresponding N_i to calculate the modified phase contribution ϕ_i

3. Use the modified phase contribution ϕ_i to calculate a new set of x_i'. Calculate difference between the initial x_i and the modified $x_i' : \delta = |x_i' - x_i|$.

4. Repeat steps (2) and (3) until for successive sets of x_i is sufficiently close to zero.

In order to perform step (2), we need to know the thickness a, which can be obtained with the following approximation:

$$a = x_{i=f} + (x_{i=f} - x_{i=f-1})/2 \qquad (7.4)$$

Where $x_i = f$ is the last mode with an effective index larger than the unknown photoactive layer refractive index at the cover interface (x=a). This requires knowledge of the minimum refractive index values in the film of interest, which can be obtained by using a surface-plasmon-mode resonance measurement [68].

To quantify the improvement due to the modified phase contribution, we use Finite-Difference Time-Domain (FDTD) calculations to construct a sample structure with a known RIP and solve for the effective indices of the guided modes. These effective index values are then used to reconstruct the RIP using the IM-IWKB method both with $\phi_i = \pi/4$, and with the modified phase contribution. We compare the accuracy of the reconstruction with and without the phase-shift correction.

7.3 NUMERICAL RESULTS AND DISCUSSION

The results of this comparison are shown in Fig. 7.1.2 and 7.2.1, which shows the reconstructed RIPs performed by the IM-IWKB method using guided mode effective indices obtained via FDTD simulation for the two cases shown in Fig. 7.1.1 – continuous (red line) and discontinuous (black line) refractive-index profile at x=a. We first consider the case where the

105

refractive profile is discontinuous at x=a (black line in Fig. 7.1.1). From Fig. 7.1.2(a) and 7.1.2(b), we see significant improvement in the agreement between the reconstruction and the actual profile when the modified phase term is used, especially for points near the interface between the photoactive layer and the cover. Averaged over the entire thickness of the photoactive layer, modifying the phase contribution reduces the root mean squared difference between the reconstruction and the actual profile from 0.01 to 0.002 in Fig. 7.1.2(a) and from 0.005 to 0.003 in Fig. 7.1.2(b). Fig. 7.1.2(c) shows that the modified IM-IWKB maintains this improved accuracy near the cover interface (x=a) even for films as thin as 500nm. Finally, Fig. 7.1.2(d) shows calculated value of ϕ_i as a function of the effective index of the mode for the structure: substrate(semi-infinite, n=1.76)/index-matched Layer (5 μm, n=1.93)/photoactive Layer (($t_{PA} = 500nm$)/cover (n=1). We see that modified phase ϕ_i (red squares) increasingly deviates from $\pi/4$ (black circles) as the effective index decreases. This makes physical sense as these lower-index modes are less strongly confined and have turning points near the interface of the photoactive layer and cover, and are therefore more strongly affected by the index/index-slope discontinuity at this interface.

In Fig. 7.2.1, we consider the case where the refractive profile is continuous at x=a (red line in Fig. 7.1.1). Fig. 7.2.1(a) shows that by introducing the modified phase contribution, we can increase the accuracy of the reconstruction, especially for modes whose turning points are near the cover interface (x=a). Fig. 7.2.1(b) shows calculated value of i as a function of the effective index of the mode for the structure: substrate (semi-infinite,

n=1.76)/index-matched Layer (5 μm, n=1.93)/photoactive Layer (t_{PA}=500 nm)/cover (n=1.8). We see that modified phase ϕ_i (red squares) increasingly deviates from $\pi/4$ (black circles) as the effective index decreases. As in the discontinuous case, this makes physical sense as these lower-index modes are less strongly confined and have turning points near the interface of the photoactive layer and cover, and are therefore more strongly affected by the index-slope discontinuity at this interface. This is also consistent with Fig. 7.1.2(a), 7.1.2(b) and Fig. 7.2.1(a), which show the most dramatic improvement at the cover interface. The modified phase term i for the continuous case is always less than $\pi/4$ (see Fig. 3(b)), whereas in the discontinuous case where the modified phase term is always greater than $\pi/4$ (see Fig. 7.1.2(d)), as can be understood by inspecting Eqs. 7.1 and 7.2.

7.4   SUMMARY AND OUTLOOK

In summary, we have developed a modified phase contribution for the IM-IWKB method [54] for the reconstruction of refractive index profiles within thin-film photovoltaic absorber layers, and quantified the improvement due to this modification for structures typical of organic photovoltaics. Near the low-index surface of the photoactive layer, this modification improves the error in the reconstructed profile from about 2% for unmodified IM-IWKB to less than 0.2% for modified IM-IWKB. Future work will apply this technique to the in-situ measurement of phase segregation evolution during the annealing of bulk heterojunction organic photovoltaics. Although we focused on the application of this technique to

organic photovoltaics, this technique applies to the reconstruction of the refractive index profile within any thin-film material.

CHAPTER 8

CONCLUSION

This thesis has presented a fundamentally new slot thin-film photovoltaic design. By allowing strong optical absorption in a photovoltaic device with a very thin active layer, the invention described in this thesis allows photovoltaics devices with improved electrical performance due to the very thin active layers (thus allowing charge to be more easily extracted from the active layer), while at the same time maintaining strong optical absorption typical of much thicker active layers in current state-of-the-art devices.

While both theoretical and computational have shown that the slot OPV structure will enhance the light absorption in the active layer, in the actual implementation, the need for high index layers make the efficient coupling of incident sunlight into the guided modes more difficult due to the reflection from high index material. In real practice, light trapping with carefully designed must be used to enable efficient coupling of the incident light into the guided mode.

We also have developed several novel characterization techniques that improve the accuracy of thin-film solar cell computational models by improving the accuracy of the input data. Both the charge collection probability and depth-depend refractive index profile reconstruction methods developed in this thesis are non-destructive and parameter-independent optoelectronic method. The self-constrained ill-posed inverse problem (SCIIP) method has the potential to improve the accuracy of inverse problem reconstruction solution in a wide range of fields, including subsurface mapping in geology [69], image reconstruction in astronomy or medicine [2, 14], and depth profiling of solar cells and other thin-film stacks [15, 55, 75]. In future work, a more efficient optimization method other than Cellular Evolutionary Algorithm should also be developed to apply this work to 2D case.

Together, these methods help us improve the measurement accuracy of the depth profile within thin-film photovoltaics for optical and electronic properties such as refractive index and charge collection probability, which is critical to the understanding, modeling and optimization of these devices.

In the future, we will focus on designing new coupling structure to couple the incidence light into the guided mode in the slot waveguide structure. For the self-constrained ill-posed inverse (SCIIP) method, we will develop a more efficient optimization method other than cellular evolution algorithm to apply this method to the 2D inverse problem.

CHAPTER 9

APPENDIX

For the code used to run the FDTD simulation. Please see the FDTD simulation package: https://github.com/wstcpyt/FDTDcpp.

For the code used to run the SCIIP method. Please see the inverse problem package: https://github.com/wstcpyt/InverseProblemPackage.

References

[1] Vilson R Almeida, Qianfan Xu, Carlos A Barrios, and Michal Lipson. Guiding and confining light in void nanostructure. *Optics letters*, 29 (11):1209–1211, 2004.

[2] Simon R Arridge. Optical tomography in medical imaging. *Inverse problems*, 15(2):R41, 1999.

[3] Ahsan Ashraf, DM Nanditha M Dissanayake, David S Germack, Conan Weiland, and Matthew D Eisaman. Confinement-induced reduction in phase segregation and interchain disorder in bulk heterojunction films. *ACS nano*, 8(1):323–331, 2013.

[4] Harry A Atwater and Albert Polman. Plasmonics for improved photovoltaic devices. *Nature materials*, 9(3):205–213, 2010.

[5] Paul WM Blom, Valentin D Mihailetchi, L Jan Anton Koster, and Denis E Markov. Device physics of polymer: fullerene bulk heterojunction solar cells. *Advanced Materials*, 19(12):1551–1566, 2007.

[6] Max Born and Emil Wolf. *Principles of optics: electromagnetic theory of propagation, interference and diffraction of light.* CUP Archive, 2000.

[7] Dennis M Callahan, Jeremy N Munday, and Harry A Atwater. Solar cell light trapping beyond the ray optic limit. *Nano letters*, 12(1):214–218, 2012.

[8] Zhuangqi Cao, Yi Jiang, Qishun Shen, Xiaoming Dou, and Yingli Chen. Exact analytical method for planar optical waveguides with arbitrary index profile. *JOSA A*, 16(9):2209–2212, 1999.

[9] KR Catchpole and Albert Polman. Plasmonic solar cells. *Optics express*, 16(26):21793–21800, 2008.

[10] Daryl M Chapin, CS Fuller, and GL Pearson. A new silicon p-n junction photocell for converting solar radiation into electrical power. *Journal of Applied Physics*, 25(5):676–677, 1954.

[11] Kin Seng Chiang. Construction of refractive-index profiles of planar dielectric waveguides from the distribution of effective indexes. *Lightwave Technology, Journal of*, 3(2):385–391, 1985.

[12] John Chilwell and Ian Hodgkinson. Thin-films field-transfer matrix theory of planar multilayer waveguides and reflection from prism-loaded waveguides. *JOSA A*, 1(7):742–753, 1984.

[13] Sarah R Cowan, Anshuman Roy, and Alan J Heeger. Recombination in polymer-fullerene bulk heterojunction solar cells. *Physical Review B*, 82 (24):245207, 2010.

[14] Ian Craig and John Brown. Inverse problems in astronomy. 1986.

[15] DM Dissanayake, Ahsan Ashraf, Yutong Pang, and Matthew D Eisaman. Mapping spatially resolved charge collection probability within p3ht: Pcbm bulk heterojunction photovoltaics. *Advanced Energy Materials*, 4(2), 2014.

[16] DMNM Dissanayake, A Ashraf, Y Pang, and MD Eisaman. Guided-mode quantum efficiency: A novel optoelectronic characterization technique. *Review of Scientific Instruments*, 83(11): 114704, 2012.

[17] C Donolato. Reconstruction of the charge collection probability in a solar cell from internal quantum efficiency measurements. *Journal of Applied Physics*, 89(10):5687–5695, 2001.

[18] PV education. Standard solar spectra, 2016. URL http://www.pveducation.org/pvcdrom/appendices/standard-solar-spectra.

[19] Heinz Werner Engl, Martin Hanke, and Andreas Neubauer. *Regularization of inverse problems*, volume 375. Springer Science & Business Media, 1996.

[20] Vivian E Ferry, Marc A Verschuuren, Hongbo BT Li, Ewold Verhagen, Robert J Walters, Ruud EI Schropp, Harry A Atwater, and Albert Polman. Light trapping in ultrathin plasmonic solar cells. *Optics express*, 18(102):A237–A245, 2010.

[21] David S Germack, Calvin K Chan, R Joseph Kline, Daniel A Fischer, David J Gundlach, Michael F Toney, Lee J Richter, and Dean M DeLongchamp. Interfacial segregation in polymer/fullerene blend films for photovoltaic devices. *Macromolecules*, 43(8):3828–3836, 2010.

[22] Martin A Green. Solar cells: operating principles, technology, and system applications. 1982.

[23] Martin A Green. The path to 25% silicon solar cell efficiency: History of silicon cell evolution. *Progress in Photovoltaics: Research and Applications*, 17(3):183–189, 2009.

[24] Martin A Green. Enhanced evanescent mode light trapping in organic solar cells and other low index optoelectronic devices. *Progress in Photovoltaics: Research and Applications*, 19(4):473–477, 2011.

[25] Wolfgang Hackbusch. *Integral equations: theory and numerical treatment*, volume 120. Birkhäuser, 2012.

[26] Behrang H Hamadani, Suyong Jung, Paul M Haney, Lee J Richter, and Nikolai B Zhitenev. Origin of nanoscale variations in photoresponse of an organic solar cell. *Nano letters*, 10(5):1611–1617, 2010.

[27] Per Christian Hansen. *Discrete inverse problems: insight and algorithms*, volume 7. Siam, 2010.

[28] M Hermle, F Granek, O Schultz, and SW Glunz. Analyzing the effects of front-surface fields on back-junction silicon solar cells using the charge-collection probability and the reciprocity theorem. *Journal of Applied Physics*, 103(5):054507, 2008.

[29] Alfons G Hoekstra, Jiri Kroc, and Peter MA Sloot. *Simulating complex systems by cellular automata*. Springer, 2010.

[30] Harald Hoppe and Niyazi Serdar Sariciftci. Organic solar cells: An overview. *Journal of Materials Research*, 19(07):1924–1945, 2004.

[31] R Jacobsson. V light reflection from films of continuously varying refractive index. *Progress in optics*, 5:247–286, 1966.

[32] R Jacobsson. Inhomogeneous and coevaporated homogeneous films for optical applications. *Physics of Thin Films*, 8:51–98, 1975.

[33] M Khardani, M Bouaïcha, and B Bessaïs. Bruggeman effective medium approach for modelling optical properties of porous silicon: comparison with experiment. *physica status solidi (c)*, 4(6):1986–1990, 2007.

[34] SS Kharintsev and M Kh Salakhov. Regularized wavelets for solving inverse ill-posed problems. In *Bayesian Inference and Maximum Entropy Methods in Science and Engineering*, volume 617, pages 259–269. AIP Publishing, 2002.

[35] Saghar Khodabakhsh, Brett M Sanderson, Jenny Nelson, and Tim S Jones. Using self-assembling dipole molecules to improve charge collection in molecular solar cells. *Advanced Functional Materials*, 16(1): 95–100, 2006.

[36] Thomas Kirchartz, Kurt Taretto, and Uwe Rau. Efficiency limits of organic bulk heterojunction solar cells. *The Journal of Physical Chemistry C*, 113(41):17958–17966, 2009.

[37] Robert Kniese, Michael Powalla, and Uwe Rau. Evaluation of electron beam induced current profiles of cu (in, ga) se 2 solar cells with different ga-contents. *Thin Solid Films*, 517(7):2357–2359, 2009.

[38] Vladimir Kochergin, Lauren Neely, Chih-Yu Jao, and Hans D Robinson. Aluminum plasmonic nanostructures for improved absorption in organic photovoltaic devices. *Applied Physics Letters*, 98(13):133305, 2011.

[39] Wee Shing Koh, Mihir Pant, Yuriy A Akimov, Wei Peng Goh, and Yuning Li. Three-dimensional optoelectronic model for organic bulk heterojunction solar cells. *Photovoltaics, IEEE Journal of*, 1(1):84–92, 2011.

[40] Christian Koos, Philipp Vorreau, Thomas Vallaitis, Pieter Dumon, Wim Bogaerts, Roel Baets, Bweh Esembeson, Ivan Biaggio, Tsuyoshi Michinobu, François Diederich, et al. All-optical high-speed signal processing with silicon–organic hybrid slot waveguides. *Nature photonics*, 3(4):216–219, 2009.

[41] LJA Koster, ECP Smits, VD Mihailetchi, and PWM Blom. Device model for the operation of polymer/fullerene bulk heterojunction solar cells. *Physical Review B*, 72(8):085205, 2005.

[42] Min-Suk Kwon and Sang-Yung Shin. Simple and fast numerical analysis of multilayer waveguide modes. *Optics communications*, 233(1):119–126, 2004.

[43] HJ Leamy. Charge collection scanning electron microscopy. *Journal of Applied Physics*, 53(6):R51–R80, 1982.

[44] M Lenes, LJA Koster, VD Mihailetchi, and PWM Blom. Thickness dependence of the efficiency of polymer: fullerene bulk heterojunction solar cells. *Applied physics letters*, 88(24):243502–243502, 2006.

[45] Gang Li, Rui Zhu, and Yang Yang. Polymer solar cells. *Nature Photonics*, 6(3):153–161, 2012.

[46] Lurng-Kuo Liu and Ephraim Feig. A block-based gradient descent search algorithm for block motion estimation in video coding. *IEEE Transactions on circuits and systems for Video Technology*, 6(4): 419–422, 1996.

[47] Olle Lundberg, Marika Edoff, and Lars Stolt. The effect of ga-grading in cigs thin film solar cells. *Thin Solid Films*, 480:520–525, 2005.

[48] RA Marsh, C Groves, and NC Greenham. A microscopic model for the behavior of nanostructured organic photovoltaic devices. *Journal of applied physics*, 101(8):083509, 2007.

[49] Alex C Mayer, Shawn R Scully, Brian E Hardin, Michael W Rowell, and Michael D McGehee. Polymer-based solar cells. *Materials today*, 10(11): 28–33, 2007.

[50] Anthony J Morfa, Kathy L Rowlen, Thomas H Reilly III, Manuel J Romero, and Jao van de Lagemaat. Plasmon-enhanced solar energy conversion in organic bulk heterojunction photovoltaics. *Applied Physics Letters*, 92(1):013504, 2008.

[51] Arnold Neumaier. Solving ill-conditioned and singular linear systems: A tutorial on regularization. *SIAM review*, 40(3):636–666, 1998.

[52] National Renewable Energy Laboratory (NREL). Reference solar spectral irradiance: Air mass 1.5, 2012. URL `http://rredc.nrel.gov/solar/spectra/am`.

[53] Inverse Problem Package. URL `https://github.com/wstcpyt/InverseProblemPackage`.

[54] YT Pang, M Bossart, and MD Eisaman. Index-matched IWKB method for the measurement of spatially varying refractive index profiles within thin-film photovoltaics. *Optics Express*, 22:A188–A197, 2014.

[55] YT Pang, H Efstathiadis, D Dwyer, and MD Eisaman. Reconstruction of the charge collection probability in a cigs solar cell by the regularization method. In *Photovoltaic Specialist Conference (PVSC), 2015 IEEE 42nd*, pages 1–4. IEEE, 2015.

[56] Yutong Pang and Matthew D Eisaman. Measuring refractive index profiles within thin-film photovoltaics with high spatial resolution using the modified im-iwkb method. pages 0655–0659, 2014.

[57] Leif AA Pettersson, Lucimara S Roman, and Olle Inganäs. Modeling photocurrent action spectra of photovoltaic devices based on organic thin films. *Journal of Applied Physics*, 86(1):487, 1999.

[58] Uwe Rau, Daniel Abou-Ras, and Thomas Kirchartz. *Advanced characterization techniques for thin film solar cells.* John Wiley & Sons, 2011.

[59] Peter N Saeta, Vivian E Ferry, Domenico Pacifici, Jeremy N Munday, and Harry A Atwater. How much can guided modes enhance absorption in thin solar cells? *Optics Express*, 17(23):20975–20990, 2009.

[60] Pablo Sanchis, Javier Blasco, Alejandro Martínez, and Javier Martí. Design of silicon-based slot waveguide configurations for optimum nonlinear performance. *Journal of Lightwave Technology*, 25(5): 1298–1305, 2007.

[61] R Scheer, C Knieper, and L Stolt. Depth dependent collection functions in thin film chalcopyrite solar cells. *Applied physics letters*, 67(20): 3007–3009, 1995.

[62] R Scheer, M Wilhelm, HJ Lewerenz, HW Schock, and L Stolt. Determination of charge carrier collecting regions in chalcopyrite heterojunction solar cells by electron-beam-induced current measurements. *Solar energy materials and solar cells*, 49(1):299–309, 1997.

[63] Frank Schmidt and David Yevick. Discrete transparent boundary conditions for schrödinger-type equations. *Journal of Computational Physics*, 134(1):96–107, 1997.

[64] LP Shi, EYB Pun, and PS Chung. Extended iwkb method for determination of the refractive-index profile in optical waveguides. *Optics letters*, 20(15):1622–1624, 1995.

[65] William Shockley and Hans J Queisser. Detailed balance limit of efficiency of p-n junction solar cells. *Journal of applied physics*, 32(3): 510–519, 1961.

[66] FDTD simulation package. URL https://github.com/wstcpyt/FDTDcpp.

[67] Lumerical Solution. URL http://www.lumerical.com/tcad-products/fdtd/.

[68] Yijun Tang, Xiangqun Zeng, and Jennifer Liang. Surface plasmon resonance: An introduction to a surface spectroscopy technique. *Journal of chemical education*, 87(7):742–746, 2010.

[69] Albert Tarantola. *Inverse problem theory and methods for model parameter estimation*. siam, 2005.

[70] Alfred Thelen. Design of multilayer interference filters. *Physics of thin films*, 5:47–86, 1969.

[71] PK Tien, R Ulrich, and RJ Martin. Modes of propagating light waves in thin deposited semiconductor films. *Applied Physics Letters*, 14(9): 291–294, 1969.

[72] Andre Nikolaevich Tikhonov and AV Goncharsky. Ill-posed problems in the natural sciences. *Ill-posed problems in the natural sciences, Moscow: MIR Publishers, 1987, 344 p., Advances in science and technology in the USSR. Mathematics and mechanics series*, 1, 1987.

[73] Andre Nikolaevich Tikhonov, AV Goncharsky, VV Stepanov, and Anatoly G Yagola. *Numerical methods for the solution of ill-posed problems*, volume 328. Springer Science & Business Media, 2013.

[74] Lloyd N Trefethen and David Bau III. *Numerical linear algebra*, volume 50. Siam, 1997.

[75] Enis Tuncer and Sidney B Lang. Numerical extraction of distributions of space-charge and polarization from laser intensity modulation method. *Applied Physics Letters*, 86(7):071107, 2005.

[76] R Ulrich and R Torge. Measurement of thin film parameters with a prism coupler. *Applied Optics*, 12(12):2901–2908, 1973.

[77] Feng Xiang and Gar Lam Yip. A modified wkb method for the improved phase shift at a turning point. *Lightwave Technology, Journal of*, 12(3):443–452, 1994.

[78] P Yeh. Wiley-interscience; hoboken, nj: 2005. *Optical waves in layered media*.

[79] Pochi Yeh. *Optical waves in layered media*, volume 95. Wiley New York, 1988.

[80] Pochi Yeh. *Optical waves in layered media*, volume 61. Wiley-Interscience, 2005.

[81] Gang Yu, Jun Gao, Jan C Hummelen, Fred Wudl, and Alan J Heeger. Polymer photovoltiac cells: Enhanced efficiencies via a network of internal donor-acceptor heterojunctions. *Science*, 270(5243):1789, 1995.

[82] Zongfu Yu, Aaswath Raman, and Shanhui Fan. Fundamental limit of nanophotonic light trapping in solar cells. *Proceedings of the National Academy of Sciences*, 107(41):17491–17496, 2010.

[83] Matei Zaharia, Mosharaf Chowdhury, Michael J Franklin, Scott Shenker, and Ion Stoica. Spark: cluster computing with working sets. In *Proceedings of the 2nd USENIX conference on Hot topics in cloud computing*, volume 10, page 10, 2010.

[84] Ying Zheng, Robel Bekele, Jiaomin Ouyang, and Jiangeng Xue. Interdigitated bulk heterojunction organic photovoltaic cells with aligned copper phthalocyanine nanorods. *Selected Topics in Quantum Electronics, IEEE Journal of*, 16(6):1544–1551, 2010.

[85] Haidong Zhu, Zhuangqi Cao, and Qishun Shen. Construction of refractive-index profiles of planar waveguides with additional information obtained from surface plasmon resonance. *Applied optics*, 44 (16):3174–3178, 2005.